1 # Phospho-tuning immunity through Denisovan, modern human and mouse
2 # TNFAIP3 gene variants

3

4 **Authors:** Nathan W. Zammit[1]*, Owen M. Siggs[1,2]*, Paul Gray[3,4], Keisuke Horikawa[5],
5 Stephen R. Daley[5^], David B. Langley[1], Daniele Cultrone[1], Elisabeth K. Malle[1], Stacey N.
6 Walters[1], Jeanette E. Villanueva[1], Joanna Warren[1], Amanda Russell[1], Mark J. Cowley[1,16],
7 Velimir Gayevskiy[1], Marcel E. Dinger[1,16], Claudia Loetsch[1], Cecile King[1], Robert Brink[1],
8 David Zahra[1], Geeta Chaudhri[5^], Gunasegaran Karupiah[5^], Belinda Whittle[5], Carla Roots[5],
9 Edward Bertram[5], Michiko Yamada[5], Yogesh Jeelall[5], Anselm Enders[5], Benjamin E. Clifton[6],
10 Peter D. Mabbitt[6], Colin J. Jackson[6], Susan R. Watson[7], Craig N. Jenne[7^], Lewis L. Lanier[7],
11 Tim Wiltshire[8], Matthew H. Spitzer[9^], Garry P. Nolan[9], Frank Schmitz[10], Alan Aderem[10],
12 Benjamin T. Porebski[11], Ashley M. Buckle[11], , Derek W. Abbott[12], John B. Ziegler[3,4], Maria
13 E. Craig[13,4], Paul Benitez-Aguirre[13], Juliana Teo[13], Melanie Wong[13], Murray P. Cox[14],
14 Wilson Phung[15], Ingrid E. Wertz[15], Daniel Christ[1,16], Christopher C. Goodnow[1,16]*†, Shane T.
15 Grey[1,16]*†

16 **Affiliations:**

17 [1]Garvan Institute of Medical Research, 384 Victoria St, Darlinghurst, New South Wales,
18 2010 Australia

19 [2]Flinders University, Bedford Park, South Australia, 5042 Australia.

20 [3]Sydney Children's Hospital, Randwick NSW, Australia.

21 [4]School of Women's and Children's Health, University of New South Wales, Sydney,
22 Australia

23 [5]John Curtin School of Medical Research, The Australian National University, Canberra,
24 Australian Capital Territory, 2601 Australia.

25 [6]Research School of Chemistry, The Australian National University, Acton, Canberra,
26 Australian Capital Territory, 2601 Australia.

27 [7]Department of Microbiology and Immunology and the Parker Institute for Cancer
28 Immunotherapy, University of California San Francisco, Parnassus Ave, San Francisco,
29 California, 94143 USA.

30 [8]Eshelman School of Pharmacy, University of North Carolina, Chapel Hill, NC 27599;

31 [9]Department of Microbiology & Immunology, Stanford University, California, 94350, USA.

32 [10]Seattle Biomedical Research Institute, Seattle, Washington, 98109-5219 USA.

33 [11]Department of Biochemistry and Molecular Biology, Monash University, Clayton, Victoria
34 3800 Australia.

35 [12]Department of Pathology, Case Western Reserve University School of Medicine,
36 Cleveland, Ohio 44106

37 [13]The Children's Hospital at Westmead, and Discipline of Child and Adolescent Health,
38 University of Sydney, Australia.

39 [14]Institute of Fundamental Sciences, Massey University, Palmerston North, New Zealand.

40 [15]Genentech Inc., 1 DNA Way, M/S 40 South San Francisco, California, 94080, USA.

[16]St Vincent's Clinical School, The University of New South Wales Sydney, New South Wales, 2010 Australia.

^present address: SD, Department of Biochemistry and Molecular Biology, Monash University, Clayton, Victoria 3800 Australia; GC, Research School of Population Health, The Australian National University, Canberra, Australian Capital Territory, 2601 Australia; & GK, School of Medicine, The University of Tasmania, Hobart, TAS 7000, Australia; CJ, Snyder Institute for Chronic Diseases, University of Calgary, AB T2N 4N1; MHS, Departments of Otolaryngology and Microbiology & Immunology and the Parker Institute for Cancer Immunotherapy, University of California San Francisco, Parnassus Ave, San Francisco, California, 94143 USA; FS, Celgene, 1616 Eastlake Ave E, Seattle, USA.

†Corresponding authors: Email c.goodnow@garvan.org.au (C.C.G.) or s.grey@garvan.org.au (S.T.G.)

*These authors contributed equally to this work.

Abstract:

54
55 Resisting or tolerating microbes are alternative strategies to survive infection, but little is
56 known about the evolutionary mechanisms controlling this balance. Here, genomic analyses
57 of anatomically modern humans, extinct Denisovan hominins, and mice revealed a series of
58 missense variants in the immune response inhibitor A20 (encoded by *TNFAIP3*), substituting
59 non-catalytic residues of the ubiquitin protease domain to diminish IκB-dependent
60 phosphorylation and activation of A20. Two A20 variants with partial phosphorylation
61 deficits appeared beneficial: one originating in Denisovans and introgressed in modern
62 humans throughout Oceania, and another in a mouse strain resistant to Coxsackievirus. By
63 contrast, a variant with 95% loss of phosphorylation caused spontaneous inflammatory
64 disease in humans and mice. Analysis of the partial phosphorylation variant in mice revealed
65 diminished tolerance of bacterial lipopolysaccharide or to poxvirus inoculation as trade-offs
66 for enhanced immunity.

67

One Sentence Summary:

68
69 Modern and ancient variants reveal a genetically tunable element for balancing immunity and
70 microbial tolerance.

Main Text:

Microbial resistance involves innate and adaptive immune responses that prevent, diminish, or clear infection, often causing collateral damage to host tissues and increased energy demands. Studies in plants[1], and more recently in animals[2,3], have shown that in some circumstances it can be more efficient for a host to tolerate microbes rather than resist them. Microbial tolerance involves homeostatic mechanisms to raise thresholds for initiating immune responses, to physically separate microbes from host immune receptors, and to repair damage caused directly by microbes or by collateral inflammation[3-6]. The genetic means by which microbial resistance and tolerance are balanced remains incompletely understood. Population genetic modelling predicts that resistance traits favor host polymorphism and microbial evasion, whereas microbial tolerance traits tend towards fixation in hosts and microbial mutualism[7]. High mortality in indigenous human populations of Oceania and the Americas exposed to smallpox demonstrate how a tolerated pathogen in its adapted host can cause devastating disease when introduced into non-adapted populations[8,9]. An example in animals can be seen for European rabbits exposed to myxoma poxvirus originating from South American rabbits[8]. These cases illustrate the importance of fine-tuning microbial immunity and tolerance during co-evolution of host and microbe, although little is known about the molecular pathways which underpin it.

A binary perspective of the importance of balancing microbial immunity and tolerance comes from Mendelian gene variants in mice and humans that completely inactivate the function of one or both alleles of genes such as *CTLA4, IL10, FOXP3,* or *TNFAIP3*[10-12]. These cause severe pediatric autoimmune or inflammatory disease, particularly at mucosal barriers where large microbial populations are normally tolerated, such as the microbial burden that drives inflammatory pathology in mouse *Tnfaip3* deficiency[6]. Genome-wide and candidate association studies in humans implicate variants at or near the *TNFAIP3* locus with susceptibility to autoimmune disease[13]. In contrast to these disease-associated traits, few examples of beneficial genetic adjustments that decrease microbial tolerance in favor for heightened immunity exist.

A20, encoded by the *TNFAIP3* gene, promotes microbial tolerance as a negative regulator of NF-κB signaling: an evolutionarily ancient and central pathway for activating innate and adaptive immune responses[13]. A20 has multiple domains with inhibitory activity against NF-κB, primarily preventing activation of the central IκB kinase (IKK) by upstream proteins RIPK1, TRAF6 and NEMO. The A20 ovarian tumor (OTU) domain is a deubiquitin (DUB) protease that cleaves activating K63-linked ubiquitin chains from RIPKI, TRAF6 or NEMO[14-16]. The A20 zinc finger 7 domain (ZnF7) binds linear polyubiquitin to suppress IKK activation, whereas ZnF4 promotes ligation of K48-linked ubiquitin chains to RIPK1, triggering RIPK1 proteolysis[14,17]. A20 feedback inhibition is induced at two levels: NF-κB proteins directly induce *TNFAIP3* mRNA, and the inhibitory activities of A20 protein are enhanced by IκKβ-induced serine phosphorylation near the ZnF domains, notably S381[18,19].

The role of the A20 OTU domain nevertheless remains enigmatic. The ZnF domains alone are sufficient for NF-κB inhibitory function in cell-based studies[20,21], and mice homozygous for *TNFAIP3* missense variants creating a catalytically inactive OTU domain have little[15,18] or no evidence[20] of excessive NF-κB signaling. Here we demonstrate that anatomically modern human, archaic Denisovan, and mouse missense variants in the OTU domain modulate A20 phosphorylation by IKK, serving as a genetically tunable element with profound effects on the balance between microbial tolerance and immunity, and evidence of introgression to high frequencies during human history.

Modern human A20 OTU variants acquired from Denisovans

Three convergent sequencing studies led us to a unique functional class of A20 missense variants affecting the OTU domain, separate from the ubiquitin protease catalytic site (Fig. 1A, B; Extended Data Fig. 1). The most subtle allele, comprising T108A (rs376205580 g.138196008A>G) and I207L (rs141807543 g.138196957A>C) missense variants in *cis*, was identified by whole genome sequencing in four of 85 families in Sydney. The majority of individuals in our cohort carrying the T108A;I207L allele were healthy family members of Māori or Pacific Islander ancestry. These variants were rare in a public variant collection (gnomAD r2.0.2) but most frequent among individuals with an unassigned ancestry (Extended Data Fig. 2A).

We traced the global distribution of the T108A;I207L allele in 279 individuals from the Simons Genome Diversity Project dataset[22], revealing high frequencies ranging from 25-75% among people of Island Southeast Asia and Oceania, but an absence of the allele elsewhere in the world (Extended Data Fig. 2B, Extended Data Table 1).

Unlike Africans or Eurasians, people in Island Southeast Asia and Oceania acquired up to 5% of their genome from Denisovans: archaic hominins that interbred with modern humans ~50,000 years ago migrating through Asia to settle the continent of Sahul (now Papua New Guinea and Australia)[23-26]. Analysis of the high-coverage genome of a Denisovan finger phalanx from a cave in the Altai Mountains of Siberia[27] revealed homozygous T108A;I207L variants (Fig. 1C). Both variants were absent from the genome of a Neanderthal who had inhabited the same cave[28] (Extended Data Table 2), suggesting that T108A and I207L arose after the divergence of Denisovan and Neanderthal lineages 170,000-700,000 years ago[27].

Multiple Denisovan-derived genomic regions, including one encompassing *TNFAIP3*, bear strong signatures of introgression in Papuans[25,26,29]. By imputing haplotypes (Extended Data Table 2) using genotype array data from 514 individuals from indigenous populations across Island Southeast Asia and Oceania[30], we found evidence that the Denisovan *TNFAIP3* haplotype has reached high frequencies in populations east of the Wallace Line, a 50 million year-old faunal boundary separating organisms of Asiatic and Australian origin via deep water channels between the two continental shelves (Fig. 1D, E and Extended Data Fig. 3)[31]. Frequencies ranged from 0% in almost all populations west of the Wallace Line, but reached 100% in 8 Baining individuals from eastern Papua New Guinea. We observed the same haplotype in 31/144 (22%) of exome-sequenced alleles in Martu Indigenous Australians from the Pilbara region of Western Australia[32], implying the haplotype enrichment occurred before the isolation of Indigenous Australian and Papuan populations. The high frequency in Polynesia indicates the Denisovan *TNFAIP3* haplotype was retained after admixture with Austronesian farming populations expanding from mainland Asia starting ~4,000 years ago[33] in Eastern Indonesia and ~3,000 years ago in the Southwest Pacific[34].

Aside from the two missense variants in the introgressed Denisovan *TNFAIP3* haplotype, many other non-coding variants could conceivably modulate transcription. Deep sequencing of cDNA nevertheless revealed equal amounts of *TNFAIP3* mRNA from Denisovan and modern human alleles in heterozygous leukocytes, with or without TNFα stimulation (Extended Data Fig. 4). Of the two coding variants, T108A was not predicted computationally to alter A20 function (Phred-scaled CADD score of 0.002) and occurs in other vertebrate species (Extended Data Fig. 1). By contrast, I207 is invariant across most jawed vertebrates, and I207L was predicted to be the most deleterious variant across the Denisovan *TNFAIP3* haplotype (Phred-scaled CADD score: 23.2; Extended Data Fig. 3E).

A mouse A20 OTU variant confers heightened resistance to Coxsackievirus

The results above identify an ancient substitution in the A20 OTU domain as apparently beneficial in human history. Further evidence that A20 OTU domain variants could be beneficial came from another OTU substitution, I325N, identified in a genome-wide mouse mutagenesis screen segregating with increased frequencies of circulating CD44^{hi} activated/memory T cells and regulatory T cells (Fig. 2A) in otherwise healthy adult mice. Detailed analysis revealed the I325N mutation also increased numbers of B cells in the spleen and peritoneal cavity, and diminished IκBα within B cells, CD8 T cells, NK cells and dendritic cells (Fig. 2B and Extended Data Fig. 5). Macrophages immortalized from bone marrow of I325N mutant mice produced more inflammatory cytokines in response to lipopolysaccharide (LPS) than controls from wild-type mice (Extended Data Fig. 6). In thymocytes, I325N increased TNFα-induced NF-κB signaling in ways consistent with diminished A20-mediated inhibition (Extended Data Fig. 7)[18].

In wild-type mice transplanted with mixtures of mutant and wild-type A20 bone marrow, the I325N mutation acted cell autonomously to increase B cell activation and proliferation by LPS or antigen receptors, and to increase TCR and CD28-dependent formation of FOXP3^{+} CD4^{+} regulatory T cells and their Helios^{+} FOXP3^{-} precursors within the thymus (Fig. 2C, D, Extended Data Fig. 8). Surprisingly, I325N had a greater effect than the C103A OTU domain mutation analyzed in parallel bone marrow transplant recipients, despite C103A completely inactivating the polyubiquitin protease activity of A20[15,20], indicating I325N must diminish additional inhibitory mechanisms.

Consistent with heightened cellular markers of immunity, I325N mutant mice had greater resistance to Coxsackievirus B4 strain E2, a virus isolated from a human neonate with a disseminated fatal infection causing extensive pancreatic necrosis[35,36]. A virus dose that was lethal for 90% of wild-type C57BL/6 mice was not lethal for *Tnfaip3*[I325N/I325N] littermates, and caused less mortality in *Tnfaip3*[I325N/+] mice (Fig. 2E; Extended Data Fig. 9A). Mutant mice had less infectious virus and viral RNA in the pancreas, less mRNA encoding immune response cytokines IL-1β and IFNβ, less pancreatic necrosis, higher serum IL-6, and preserved body-weight and euglycemia (Fig. 2F, G; Extended Data Fig. 9B-G).

The homogeneous genetic background of I325N mutant mice allowed testing if heightened immunity imposed a subclinical cost or altered the insulin anabolic axis[37]. *Tnfaip3*[I325N/+] mice were healthy, of normal weight, and fertile, producing homozygous mutant offspring at the expected ratio. Homozygotes also appeared healthy, although their body weight was 5-20% less than heterozygous or wild-type littermates (Fig. 3A), with histological analysis revealing low-grade inflammation of the pancreatic islets, colon, kidney, and liver (Fig. 3B-C, Extended Data Fig. 10). Pancreatic insulitis in I325N homozygotes was associated with a 50% reduction in beta cell mass (Fig. 3D), although random blood glucose levels and glucose tolerance tests were normal (Extended Data Fig. 11A-E). Isolated *Tnfaip3*[I325N/I325N] islets exhibited normal basal insulin output but reduced insulin secretion when stimulated *in vitro* (Extended Data Fig. 11F). Islet transplant and culture experiments showed the A20 mutation acted within islet cells, exaggerating canonical and non-canonical NF-κB signaling, lowering insulin secretion, and increasing inflammatory cytokine production (Fig. 3E-H and Extended Data Fig. 11G-I & 12)[38].

An allelic series of OTU domain variants with graded reductions of A20 phosphorylation

The apparent beneficial effects of the T108A;I207L and I325N OTU domain substitutions above contrasted with a third OTU domain substitution, C243Y, found as a family-specific variant causing dominant Mendelian inflammation resembling Behçet's disease, with childhood-onset oral and genital ulceration and skin inflammation[39]. The biochemical basis for the clinically penetrant effects of C243Y was obscure, because other similarly affected cases of haploinsufficiency of A20 (HA20) result from nonsense or frameshift variants that truncate or eliminate A20 protein[12].

Despite different clinical consequences, the three OTU domain variants formed a graded biochemical allelic series when full-length A20 and IKKβ were co-expressed in mouse insulinoma cells and S381-phosphorylated A20 was compared with total A20 protein by Western blotting. None of the variants affected A20 protein accumulation but each affected IKKβ-mediated S381 phosphorylation (Fig. 4A-C; Extended Data Fig. 13A). The pathogenic C243Y variant caused the most severe loss of function, diminishing IKKβ-mediated S381 phosphorylation to 5% of wild-type, whereas the Denisovan T108A;I207L variant diminished phosphorylation the least (80% of wild-type) and the non-pathogenic I325N variant had an intermediate effect (50% of wild-type). By contrast, the C103A catalytic site substitution did not cause a significant decrease in A20 phosphorylation. Loss of S381 phosphorylation was also observed by mass spectrometry of A20 purified from unstimulated human cells transfected with $A20^{I325N}$ compared to $A20^{WT}$, whereas $A20^{C103A}$ exhibited normal phosphorylation (Extended Data Fig. 13B).

S381-phosphorylated A20 predominantly migrated more slowly in SDS-PAGE than unphosphorylated A20, either when tested by co-transfection with IKKβ (Fig. 4A, B) or in TNFα-stimulated peripheral blood leukocytes with endogenous A20 and IKKβ (Fig. 4D, S14). The ratio of this slowly migrating A20 species to the more rapidly migrating form was markedly decreased in blood leukocytes from healthy donors heterozygous for the Denisovan T108A;I207L variants, and further decreased in a healthy T108A;I207L homozygous donor, compared to healthy controls without these variants (Fig. 4E). The ratio of phosphorylated-S381 to fast-migrating A20 was also decreased (Extended Data Fig. 14F). TNF-α stimulated leukocytes from variant carriers also had heightened expression of NF-κB-induced transcripts of *ICAM1*, *CXCL2, TNF*, and *TNFAIP3* itself (Extended Data Fig. 15), and a trend towards reduced IκBα protein levels (Extended Data Fig. 14H).

When A20 was measured for inhibition of an NF-κB luciferase reporter in unstimulated or TNFα-stimulated mouse insulinoma cells, inhibition was diminished in a graded fashion by each OTU domain variant in the same order that these diminished S381 phosphorylation (Fig. 4F; Extended Data Fig. 13C). The deleterious C243Y variant was the most compromised inhibitor of the series, almost as compromised as A20 with S381 substituted to non-phosphorylatable alanine (S381A). Combining the intermediate I325N mutation with a S381A mutation *in cis* did not cause a further decrease in A20 inhibition, consistent with I325N having its effect upon phosphorylation. That conclusion was reinforced by combining I325N *in cis* with a substitution of S381 to the phosphoserine mimetic glutamate (S381E), which rescued the lost activity caused by I325N (Extended Data Fig. 13D, E). Testing the two Denisovan variants individually, T108A had no measurable effect whereas I207L diminished A20 inhibitory activity comparably to the two variants combined (Extended Data Fig. 13F), supporting I207L as the functional variant within the introgressed Denisovan haplotype.

259   To explore the structural and biochemical consequences of variants on the posterior surface
260   of the OTU domain, we focused on the intermediate I325N allele. Crystallographic structures
261   of A20 OTU domains with wild-type I325 or mutant N325 revealed no differences in features
262   with known functions, including the catalytic triad and ubiquitin-binding surface (Fig. 1B;
263   Extended Data Fig. 16A-C). I325N also did not alter the conserved posterior surface of the
264   OTU domain[40], including the β3-β4 loop containing C243 (Extended Data Fig. 16G),
265   although there were subtle shifts in the stem of the β7-β8 loop, which contains conserved
266   surface residues T321, T322 and L324 (Extended Data Fig. 16D-G). The β7-β8 loop itself is
267   disordered in all available OTU structures but, like the disordered loops in the unliganded S1
268   ubiquitin-binding site, it may undergo conformational changes upon binding a cognate
269   partner that are hindered by the I325N variant. Wild-type and variant OTU domains exhibited
270   similar thermal denaturation profiles (Extended Data Fig. 17A-C), and the corresponding
271   full-length proteins were comparably stable in cycloheximide-treated mammalian cells
272   (Extended Data Fig. 17D). I325N did not decrease DUB activity of bacterially expressed
273   OTU domain against K48-polyubiquitin *in vitro* (Extended Data Fig. 17E-G), but I325N
274   diminished K63-polyubiquitin DUB activity and K48-ubiquitin ligase activity when full
275   length A20 was expressed in human cells (Extended Data Fig. 17H, I) consistent with these
276   activities requiring S381 phosphorylation[18,19].

277

Shift from beneficial to detrimental loss of microbial tolerance

279   We next explored the possibility that partial loss of A20 phosphorylation and subclinical loss
280   of microbial tolerance might become detrimental in particular environmental or genetic
281   settings. In an experimental model for septic shock, I325N homozygous mice had increased
282   IL-6 production and high mortality following injection of a dose of bacterial LPS that was not
283   lethal in wild-type controls (Fig. 5A, B). In the rodent counterpart of smallpox, infection with
284   the orthopoxvirus ectromelia virus was tolerated and controlled by wild-type mice, yet
285   resulted in high mortality and higher viral titres in I325N homozygotes (Fig. 5C, D and
286   Extended Data Fig. 18). In bone marrow chimeric mice with a higher frequency of pancreatic
287   islet-reactive CD4^{+} T cells , autoreactive T cells escaped deletion and precipitated diabetes
288   when half the hematopoietic cells were homozygous for I325N (Extended Data Fig. 19A-C).
289   The rogue islet-reactive T cells were nevertheless derived equally from A20 wild-type or
290   I325N precursors, whereas I325N acted cell autonomously to increase MHC II and the T cell
291   costimulator CD86 on B cells and dendritic cells and to increase frequencies of germinal
292   centre B cells (Extended Data Fig. 19D-F).

293   While specific stressors were required to reveal detrimental effects of the intermediate I325N
294   variant, wasting disease occurred spontaneously in young C57BL/6 mice homozygous for the
295   severe C243Y variant. C243Y homozygotes were born at the expected Mendelian ratio but
296   compared to wild-type littermates failed to thrive, exhibiting a large reduction in body weight
297   and early lethality (Fig. 5E, F; Extended Data Fig. 20). Surviving C243Y homozygotes
298   showed intestinal pathology including loss of goblet cells responsible for sustaining the
299   mucin barrier between epithelium and microbes of the intestinal lumen, along with an
300   increased frequency of circulating CD44^{hi} activated/memory T cells (Extended Data Fig. 20).
301   C243Y homozygous mice thus resemble A20-null mice[5,11], paralleling the clinical similarity
302   between C243Y missense and A20 loss-of-function variants in heterozygous humans[12].

Discussion

Our findings reveal genetic and biochemical mechanisms for adaptively increasing immunity, with trade-offs against microbial tolerance and anabolic metabolism that either remain clinically silent or become detrimental in specific contexts. Three different missense alleles in the N-terminal A20 OTU domain act, to different degrees, by diminishing A20 phosphorylation and tuning down A20's immune inhibitory activity. A rare human variant, C243Y, diminishes phosphorylation almost entirely and shifts the balance away from microbial tolerance to the extremes of immunity, resulting in severe inflammatory disease in both mice and humans. This outcome is comparable with other human variants that eliminate or truncate A20 protein from one *TNFAIP3* allele or engineered mouse variants that eliminate A20 from both alleles[11,12]. By contrast, I325N and I207L variants decrease A20 phosphorylation more modestly, without precipitating spontaneous inflammatory disease in the mice or humans who harbor them. I325N in the mouse confers dramatically increased resistance to an otherwise lethal dose of a Coxsackievirus. A similar resistance to microbial pathogens may explain the beneficial effect of Denisovan I207L, as evidenced by its high frequency in modern human populations east of the Wallace Line, who likely encountered new infectious agents as they moved into environments with unique fauna and flora.

Previous studies in mice have conditionally deleted A20 in specific tissues, causing severe inflammatory disease, or directly disabled individual enzymatic functions of A20 in all tissues resulting in surprisingly little inflammation[5,6,11,15,18,20]. By contrast, OTU domain variants tuning phosphorylation regulate multiple ubiquitin-editing functions of A20[18,19], and as shown here have greater effects on microbial tolerance and resistance *in vivo* than variants affecting individual ubiquitin-editing activities. The C243Y and I325N variants involve buried residues in two separate surface loops, β3-β4 and β7-β8 respectively (Extended Data Fig. 16), on the highly conserved posterior surface of the OTU domain[40]. Structural studies of full-length A20 protein may illuminate how this surface relates to the C-terminal domain carrying S381. Because the conserved surface bounded by C243Y and I325N is large, it potentially offers many opportunities for substitution of buried or surface residues to tune immunity and tolerance.

Our study of the intermediate loss-of-function A20 variant, I325N, provides two examples of genetic trade-offs. The first was with glucose metabolism, where *Tnfaip3*[I325N] had the surprising effect within pancreatic islet beta cells of decreasing insulin secretion while increasing inflammation. This is reminiscent of findings in *Drosophila* that insulin production or action decreases during infection, diminishing body glycogen supplies through increased FOXO activity, a transcriptional inducer of starvation responses[37]. Resting insulin levels are a good prognostic marker in human sepsis, and exogenous insulin treatment improves outcome[41]. Subtly decreased A20 activity may enhance immune demands for energy and, separately, help meet these energy demands by lowering insulin-induced anabolic growth, both contributing to cachexia associated with chronic infection and inflammation.

The second example of a trade-off is the experimental demonstration that a beneficial trait in one context can be deleterious in another. *Tnfaip3*[I325N] conferred increased resistance to Coxsackievirus, an important human enterovirus, but increased mortality to ectromelia virus, a relative of variola and myxoma viruses. Higher ectromelia virus mortality in *Tnfaip3*[I325N] mice is reminiscent of the high mortality in indigenous populations of the Americas and Oceania exposed to variola virus relative to Europeans[8]. The findings here suggest that the devastation wrought by these and other microbes reflects selection during earlier environmental conditions for lower microbial tolerance and a stronger immune response, with A20 representing one critical determinant of this outcome.

References and Notes:

Main text references 1-42

1   Caldwell, R. M., Schafer, J. F., Compton, L. E. & Patterson, F. L. Tolerance to Cereal Leaf Rusts. *Science* **128**, 714-715, doi:10.1126/science.128.3326.714 (1958).

2   Ayres, J. S. & Schneider, D. S. Tolerance of infections. *Annu Rev Immunol* **30**, 271-294, doi:10.1146/annurev-immunol-020711-075030 (2012).

3   Soares, M. P., Teixeira, L. & Moita, L. F. Disease tolerance and immunity in host protection against infection. *Nat Rev Immunol* **17**, 83-96, doi:10.1038/nri.2016.136 (2017).

4   Hooper, L. V., Littman, D. R. & Macpherson, A. J. Interactions between the microbiota and the immune system. *Science* **336**, 1268-1273, doi:10.1126/science.1223490 (2012).

5   Vereecke, L. *et al.* A20 controls intestinal homeostasis through cell-specific activities. *Nature communications* **5**, 5103, doi:10.1038/ncomms6103 (2014).

6   Turer, E. E. *et al.* Homeostatic MyD88-dependent signals cause lethal inflammation in the absence of A20. *J Exp Med* **205**, 451-464, doi:10.1084/jem.20071108 (2008).

7   Roy, B. A. & Kirchner, J. W. Evolutionary dynamics of pathogen resistance and tolerance. *Evolution* **54**, 51-63 (2000).

8   Fenner, F. The Florey lecture, 1983. Biological control, as exemplified by smallpox eradication and myxomatosis. *Proc R Soc Lond B Biol Sci* **218**, 259-285 (1983).

9   Boughton, C. R. Smallpox and Australia. *Intern Med J* **32**, 59-61 (2002).

10   Bousfiha, A. *et al.* The 2017 IUIS Phenotypic Classification for Primary Immunodeficiencies. *J Clin Immunol* **38**, 129-143, doi:10.1007/s10875-017-0465-8 (2018).

11   Lee, E. G. *et al.* Failure to regulate TNF-induced NF-kappaB and cell death responses in A20-deficient mice. *Science* **289**, 2350-2354 (2000).

12   Zhou, Q. *et al.* Loss-of-function mutations in TNFAIP3 leading to A20 haploinsufficiency cause an early-onset autoinflammatory disease. *Nat Genet* **48**, 67-73, doi:10.1038/ng.3459 (2016).

13   Ma, A. & Malynn, B. A. A20: linking a complex regulator of ubiquitylation to immunity and human disease. *Nat Rev Immunol* **12**, 774-785, doi:nri3313 [pii]10.1038/nri3313 (2012).

14   Wertz, I. E. *et al.* De-ubiquitination and ubiquitin ligase domains of A20 downregulate NF-kappaB signalling. *Nature* **430**, 694-699, doi:10.1038/nature02794nature02794 [pii] (2004).

15   Lu, T. T. *et al.* Dimerization and ubiquitin mediated recruitment of a20, a complex deubiquitinating enzyme. *Immunity* **38**, 896-905, doi:S1074-7613(13)00146-5 [pii]10.1016/j.immuni.2013.03.008 (2013).

16   Evans, P. C. *et al.* Zinc-finger protein A20, a regulator of inflammation and cell survival, has de-ubiquitinating activity. *Biochem J* **378**, 727-734, doi:10.1042/BJ20031377BJ20031377 [pii] (2004).

17   Bosanac, I. *et al.* Ubiquitin binding to A20 ZnF4 is required for modulation of NF-kappaB signaling. *Mol Cell* **40**, 548-557, doi:S1097-2765(10)00785-9 [pii]10.1016/j.molcel.2010.10.009 (2010).

18   Wertz, I. E. *et al.* Phosphorylation and linear ubiquitin direct A20 inhibition of inflammation. *Nature* **528**, 370-375, doi:10.1038/nature16165 (2015).

19   Hutti, J. E. *et al.* IkappaB kinase beta phosphorylates the K63 deubiquitinase A20 to cause feedback inhibition of the NF-kappaB pathway. *Mol Cell Biol* **27**, 7451-7461 (2007).

20   De, A., Dainichi, T., Rathinam, C. V. & Ghosh, S. The deubiquitinase activity of A20 is dispensable for NF-kappaB signaling. *EMBO Rep* **15**, 775-783, doi:10.15252/embr.201338305 (2014).

21   Verhelst, K. *et al.* A20 inhibits LUBAC-mediated NF-kappaB activation by binding linear polyubiquitin chains via its zinc finger 7. *EMBO J* **31**, 3845-3855, doi:emboj2012240 [pii]10.1038/emboj.2012.240 (2012).

22   Mallick, S. *et al.* The Simons Genome Diversity Project: 300 genomes from 142 diverse populations. *Nature* **538**, 201-206, doi:10.1038/nature18964 (2016).

23   Reich, D. *et al.* Genetic history of an archaic hominin group from Denisova Cave in Siberia. *Nature* **468**, 1053-1060, doi:10.1038/nature09710 (2010).

24   Reich, D. *et al.* Denisova admixture and the first modern human dispersals into Southeast Asia and Oceania. *American journal of human genetics* **89**, 516-528, doi:10.1016/j.ajhg.2011.09.005 (2011).

25   Sankararaman, S., Mallick, S., Patterson, N. & Reich, D. The Combined Landscape of Denisovan and Neanderthal Ancestry in Present-Day Humans. *Curr Biol* **26**, 1241-1247, doi:10.1016/j.cub.2016.03.037 (2016).

26   Vernot, B. *et al.* Excavating Neandertal and Denisovan DNA from the genomes of Melanesian individuals. *Science* **352**, 235-239, doi:10.1126/science.aad9416 (2016).

27   Meyer, M. *et al.* A high-coverage genome sequence from an archaic Denisovan individual. *Science* **338**, 222-226, doi:10.1126/science.1224344 (2012).

410 28 Prufer, K. *et al.* The complete genome sequence of a Neanderthal from the Altai Mountains. *Nature*
411   **505**, 43-49, doi:10.1038/nature12886 (2014).
412 29 Gittelman, R. M. *et al.* Archaic Hominin Admixture Facilitated Adaptation to Out-of-Africa
413   Environments. *Curr Biol* **26**, 3375-3382, doi:10.1016/j.cub.2016.10.041 (2016).
414 30 Hudjashov, G. *et al.* Complex Patterns of Admixture across the Indonesian Archipelago. *Mol Biol Evol*
415   **34**, 2439-2452, doi:10.1093/molbev/msx196 (2017).
416 31 Wallace, A. R. On the physical geography of the Malay archipelago. *The Journal of the Royal*
417   *Geographical Society of London* **33**, 217-234 (1863).
418 32 Tang, D. *et al.* Reference genotype and exome data from an Australian Aboriginal population for
419   health-based research. *Sci Data* **3**, 160023, doi:10.1038/sdata.2016.23 (2016).
420 33 Xu, S. *et al.* Genetic dating indicates that the Asian-Papuan admixture through Eastern Indonesia
421   corresponds to the Austronesian expansion. *Proc Natl Acad Sci U S A* **109**, 4574-4579,
422   doi:10.1073/pnas.1118892109 (2012).
423 34 Skoglund, P. *et al.* Genomic insights into the peopling of the Southwest Pacific. *Nature* **538**, 510-513,
424   doi:10.1038/nature19844 (2016).
425 35 Kibrick, S. & Benirschke, K. Severe generalized disease (encephalohepatomyocarditis) occurring in the
426   newborn period and due to infection with Coxsackie virus, group B; evidence of intrauterine infection
427   with this agent. *Pediatrics* **22**, 857-875 (1958).
428 36 Hartig, P. C. & Webb, S. R. Heterogeneity of a human isolate of Coxsackie B4: biological differences.
429   *J Infect* **6**, 43-48 (1983).
430 37 Dionne, M. S., Pham, L. N., Shirasu-Hiza, M. & Schneider, D. S. Akt and FOXO dysregulation
431   contribute to infection-induced wasting in Drosophila. *Curr Biol* **16**, 1977-1985,
432   doi:10.1016/j.cub.2006.08.052 (2006).
433 38 Malle, E. K. *et al.* Nuclear factor kappaB-inducing kinase activation as a mechanism of pancreatic beta
434   cell failure in obesity. *J Exp Med* **212**, 1239-1254, doi:10.1084/jem.20150218 (2015).
435 39 Shigemura, T. *et al.* Novel heterozygous C243Y A20/TNFAIP3 gene mutation is responsible for
436   chronic inflammation in autosomal-dominant Behcet's disease. *RMD Open* **2**, e000223,
437   doi:10.1136/rmdopen-2015-000223 (2016).
438 40 Komander, D. & Barford, D. Structure of the A20 OTU domain and mechanistic insights into
439   deubiquitination. *Biochem J* **409**, 77-85, doi:BJ20071399 [pii]10.1042/BJ20071399 (2008).
440 41 van den Berghe, G. *et al.* Intensive insulin therapy in critically ill patients. *N Engl J Med* **345**, 1359-
441   1367, doi:10.1056/NEJMoa011300 (2001).
442 42 Mevissen, T. E. *et al.* Molecular basis of Lys11-polyubiquitin specificity in the deubiquitinase
443   Cezanne. *Nature* **538**, 402-405, doi:10.1038/nature19836 (2016).

References cited in Materials and Methods and Extended Data:

446 43 McKenna, A. *et al.* The Genome Analysis Toolkit: a MapReduce framework for analyzing next-
447   generation DNA sequencing data. *Genome Res* **20**, 1297-1303, doi:10.1101/gr.107524.110 (2010).
448 44 McLaren, W. *et al.* The Ensembl Variant Effect Predictor. *Genome Biol* **17**, 122, doi:10.1186/s13059-
449   016-0974-4 (2016).
450 45 MacArthur, D. G. *et al.* A systematic survey of loss-of-function variants in human protein-coding
451   genes. *Science* **335**, 823-828, doi:10.1126/science.1215040 (2012).
452 46 Paila, U., Chapman, B. A., Kirchner, R. & Quinlan, A. R. GEMINI: integrative exploration of genetic
453   variation and genome annotations. *PLoS Comput Biol* **9**, e1003153, doi:10.1371/journal.pcbi.1003153
454   (2013).
455 47 Gayevskiy, V., Roscioli, T., Dinger, M. E. & Cowley, M. J. Seave: a comprehensive web platform for
456   storing and interrogating human genomic variation. *bioRxiv*, doi:10.1101/258061 (2018).
457 48 Thorvaldsdottir, H., Robinson, J. T. & Mesirov, J. P. Integrative Genomics Viewer (IGV): high-
458   performance genomics data visualization and exploration. *Brief Bioinform* **14**, 178-192,
459   doi:10.1093/bib/bbs017 (2013).
460 49 Kircher, M. *et al.* A general framework for estimating the relative pathogenicity of human genetic
461   variants. *Nat Genet* **46**, 310-315, doi:10.1038/ng.2892 (2014).
462 50 Ho, W. Y., Cooke, M. P., Goodnow, C. C. & Davis, M. M. Resting and anergic B cells are defective in
463   CD28-dependent costimulation of naive CD4+ T cells. *J Exp Med* **179**, 1539-1549 (1994).
464 51 Akkaraju, S. *et al.* A range of CD4 T cell tolerance: partial inactivation to organ-specific antigen allows
465   nondestructive thyroiditis or insulitis. *Immunity* **7**, 255-271 (1997).
466 52 Tahiliani, V., Chaudhri, G., Eldi, P. & Karupiah, G. The orchestrated functions of innate leukocytes
467   and T cell subsets contribute to humoral immunity, virus control, and recovery from secondary
468   poxvirus challenge. *J Virol* **87**, 3852-3861, doi:10.1128/JVI.03038-12 (2013).

469	53	Wang, G. G. *et al.* Quantitative production of macrophages or neutrophils ex vivo using conditional Hoxb8. *Nat Methods* **3**, 287-293, doi:10.1038/nmeth865 (2006).
471	54	Cantley, J. *et al.* A preexistent hypoxic gene signature predicts impaired islet graft function and glucose homeostasis. *Cell Transplant* **22**, 2147-2159, doi:10.3727/096368912X658728 (2013).
473	55	Grey, S. T., Lock, J., Bach, F. H. & Ferran, C. Adenovirus-mediated gene transfer of A20 in murine islets inhibits Fas-induced apoptosis. *Transplant Proc* **33**, 577-578, doi:S0041-1345(00)02149-7 [pii] (2001).
476	56	Grey, S. T. *et al.* Genetic engineering of a suboptimal islet graft with A20 preserves beta cell mass and function. *J Immunol* **170**, 6250-6256 (2003).
478	57	Daley, S. R., Hu, D. Y. & Goodnow, C. C. Helios marks strongly autoreactive CD4+ T cells in two major waves of thymic deletion distinguished by induction of PD-1 or NF-kappaB. *J Exp Med* **210**, 269-285, doi:10.1084/jem.20121458 (2013).
481	58	Jeelall, Y. S. *et al.* Human lymphoma mutations reveal CARD11 as the switch between self-antigen-induced B cell death or proliferation and autoantibody production. *J Exp Med* **209**, 1907-1917, doi:10.1084/jem.20112744 (2012).
484	59	Bendall, S. C. *et al.* Single-cell mass cytometry of differential immune and drug responses across a human hematopoietic continuum. *Science* **332**, 687-696, doi:10.1126/science.1198704 (2011).
486	60	Bodenmiller, B. *et al.* Multiplexed mass cytometry profiling of cellular states perturbed by small-molecule regulators. *Nature biotechnology* **30**, 858-867, doi:10.1038/nbt.2317 (2012).
488	61	Qiu, P. *et al.* Extracting a cellular hierarchy from high-dimensional cytometry data with SPADE. *Nature biotechnology* **29**, 886-891, doi:10.1038/nbt.1991 (2011).
490	62	Untergasser, A. *et al.* Primer3--new capabilities and interfaces. *Nucleic Acids Res* **40**, e115, doi:10.1093/nar/gks596 (2012).
492	63	Liuwantara, D. *et al.* Nuclear factor-kappaB regulates beta-cell death: a critical role for A20 in beta-cell protection. *Diabetes* **55**, 2491-2501, doi:55/9/2491 [pii]10.2337/db06-0142 (2006).
494	64	Tan, B. M. *et al.* Baculoviral inhibitors of apoptosis repeat containing (BIRC) proteins fine-tune TNF-induced nuclear factor kappaB and c-Jun N-terminal kinase signalling in mouse pancreatic beta cells. *Diabetologia* **56**, 520-532, doi:10.1007/s00125-012-2784-x (2013).
497	65	Leslie, A. G. W. & Powell, H. R. Processing diffraction data with MOSFLM. *Nato Sci Ser Ii Math* **245**, 41-51 (2007).
499	66	Evans, P. R. An introduction to data reduction: space-group determination, scaling and intensity statistics. *Acta Crystallogr D* **67**, 282-292, doi:Doi 10.1107/S090744491003982x (2011).
501	67	Evans, P. R. & Murshudov, G. N. How good are my data and what is the resolution? *Acta Crystallogr D* **69**, 1204-1214, doi:Doi 10.1107/S0907444913000061 (2013).
503	68	Evans, P. Scaling and assessment of data quality. *Acta crystallographica. Section D, Biological crystallography* **62**, 72-82, doi:10.1107/S0907444905036693 (2006).
505	69	Winn, M. D. *et al.* Overview of the CCP4 suite and current developments. *Acta Crystallogr D* **67**, 235-242, doi:Doi 10.1107/S0907444910045749 (2011).
507	70	McCoy, A. J. *et al.* Phaser crystallographic software. *Journal of applied crystallography* **40**, 658-674, doi:10.1107/S0021889807021206 (2007).
509	71	Murshudov, G. N. *et al.* REFMAC5 for the refinement of macromolecular crystal structures. *Acta Crystallogr D* **67**, 355-367, doi:Doi 10.1107/S0907444911001314 (2011).
511	72	Adams, P. D. *et al.* PHENIX: a comprehensive Python-based system for macromolecular structure solution. *Acta crystallographica. Section D, Biological crystallography* **66**, 213-221, doi:10.1107/S0907444909052925 (2010).
514	73	Terwilliger, T. C. *et al.* Iterative-build OMIT maps: map improvement by iterative model building and refinement without model bias. *Acta crystallographica. Section D, Biological crystallography* **64**, 515-524, doi:10.1107/S0907444908004319 (2008).
517	74	Emsley, P., Lohkamp, B., Scott, W. G. & Cowtan, K. Features and development of Coot. *Acta Crystallogr D* **66**, 486-501, doi:Doi 10.1107/S0907444910007493 (2010).
519	75	Chen, V. B. *et al.* MolProbity: all-atom structure validation for macromolecular crystallography. *Acta Crystallogr D* **66**, 12-21, doi:Doi 10.1107/S0907444909042073 (2010).
521	76	Zoldak, G., Zubrik, A., Musatov, A., Stupak, M. & Sedlak, E. Irreversible thermal denaturation of glucose oxidase from Aspergillus niger is the transition to the denatured state with residual structure. *J Biol Chem* **279**, 47601-47609, doi:10.1074/jbc.M406883200 (2004).
524	77	Cowley, M. J. *et al.* Human Islets Express a Marked Pro-Inflammatory Molecular Signature Prior to Transplantation. *Cell Transplant* **21**, 2063-2078, doi:cowleyct0181 [pii]10.3727/096368911X627372 (2012).
527	78	Shim, J. H. *et al.* TAK1, but not TAB1 or TAB2, plays an essential role in multiple signaling pathways in vivo. *Genes Dev* **19**, 2668-2681, doi:gad.1360605 [pii]10.1101/gad.1360605 (2005).

548

549 **Author contributions:** Human family recruitment and genome sequence analysis: PG, JBZ,
550 MEC, PB-A, JT, MW, OMS, AR, MJC, VG, MED, CCG. Tracing Denisovan haplotype in
551 human populations by OMS, PG, AR, MPC, CCG; peripheral blood analyses by NWZ, AR,
552 CCG, STG. I325N mutation: identification by SRW, CNJ, LLL, TW, CR, BW, CCG;
553 immune cell analysis by KH, SRD, YJ, NWZ, MY, EB, AE, MHS, GPN, FS, DEZ, AA,
554 IEW, STG, CCG; Coxsackievirus studies by NWZ, CL, JW, CK, STG; Ectromelia studies by
555 GC, GK; body weight, islet, LPS and inflammation studies by NWZ, SNW, EKM, JEV,
556 STG; protease activity and structural studies by KH, NWZ, DBL, DC, WP, IEW, BEC, PDM,
557 CJJ, BTP, AMB, STG, CCG. C243Y mouse strain production and analysis by NWZ, RB,
558 DZ, SNW, DC, JW, STG. A20 phosphorylation and NF-κB luciferase analysis by NWZ, DC,
559 DWA, WP, IEW, CCG, STG.

560

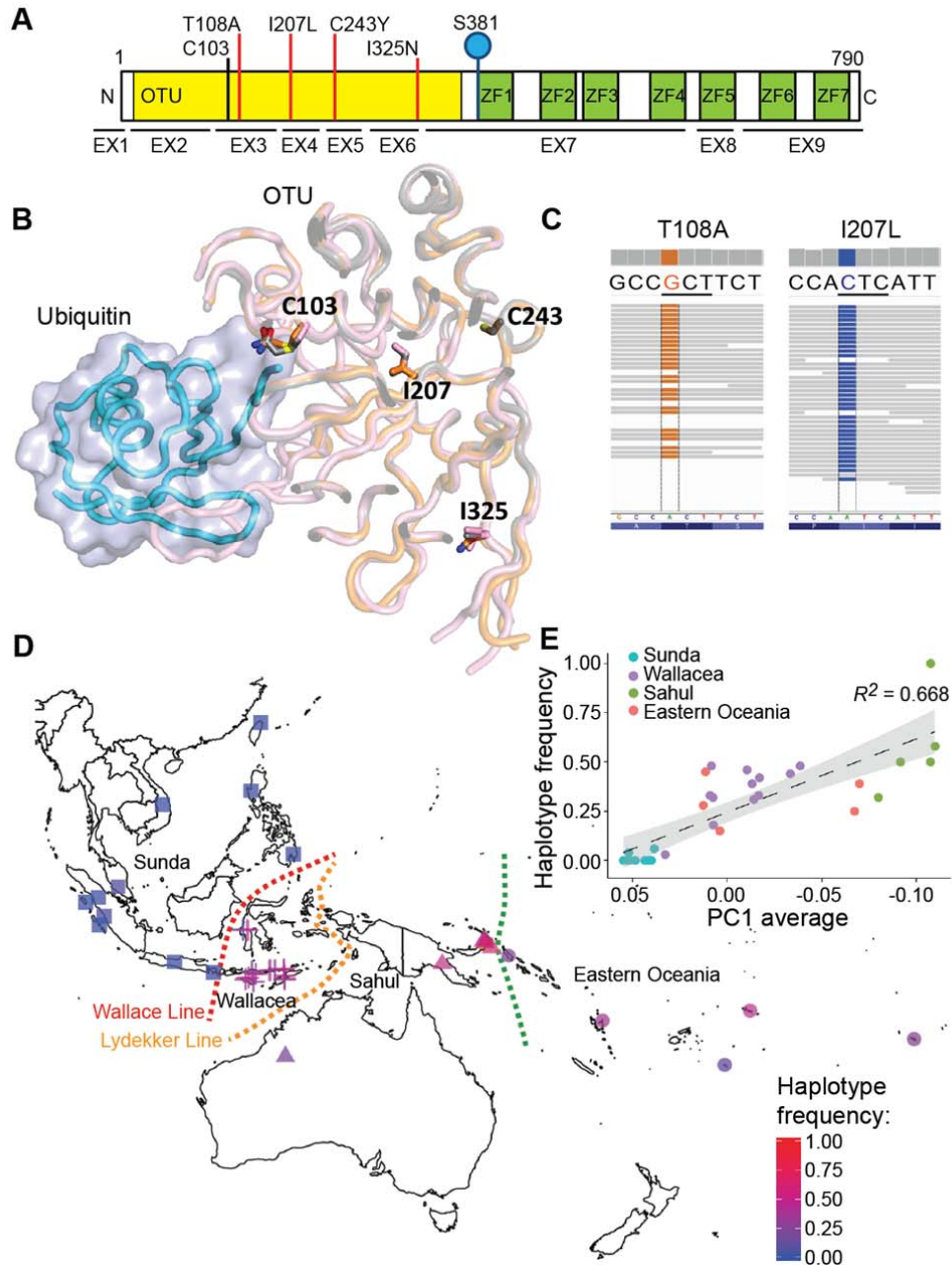561 **Competing interests:** Authors declare no competing interests.

562

563 **Data and materials availability:** All data is available in the main text or the supplementary
564 materials.

565

566 **Extended Data:**

567 Materials and Methods
568 Extended Data Figures 1-20
569 Extended Data Tables 1-5
570 References (43-78)

571

572

Fig. 1. Denisovan, modern human, and mouse variants substituting noncatalytic residues of the A20 OTU domain. (A) Schematic of A20 protein encoded by the *TNFAIP3* gene (CCDS5187), showing exons (EX1-9), ovarian tumor domain (OTU), zinc fingers (ZF1-7), OTU catalytic residue (C103), S381 phosphorylation site, and missense variants studied here (red lines). **(B)** Location of variant residues in sliced structure 5LRX[42] of A20 OTU domain (pink) complexed with ubiquitin (blue). Structures for WT and I325N OTU domains are superposed in grey and orange, respectively. **(C)** Read data of a high-coverage Denisovan genome[27] across *TNFAIP3* codons 108 and 207. **(D)** Imputed frequency of the Denisovan *TNFAIP3* haplotype in genotype array data from 514 individuals from indigenous populations across Island Southeast Asia and Oceania[30], and directly observed in exome data from 72 Martu indigenous Australians[32]. Different shape symbols group populations from

14

584 Sunda, Wallacea, Sahul and Eastern Oceania. **(E)** Imputed Denisovan *TNFAIP3* haplotype
585 frequency from populations described in (D) (filled circles) versus a surrogate estimate of
586 Papuan ancestry (principal component 1, Extended Data Fig. 3). Gray shading indicates 95%
587 confidence interval of linear regression line.
588

589
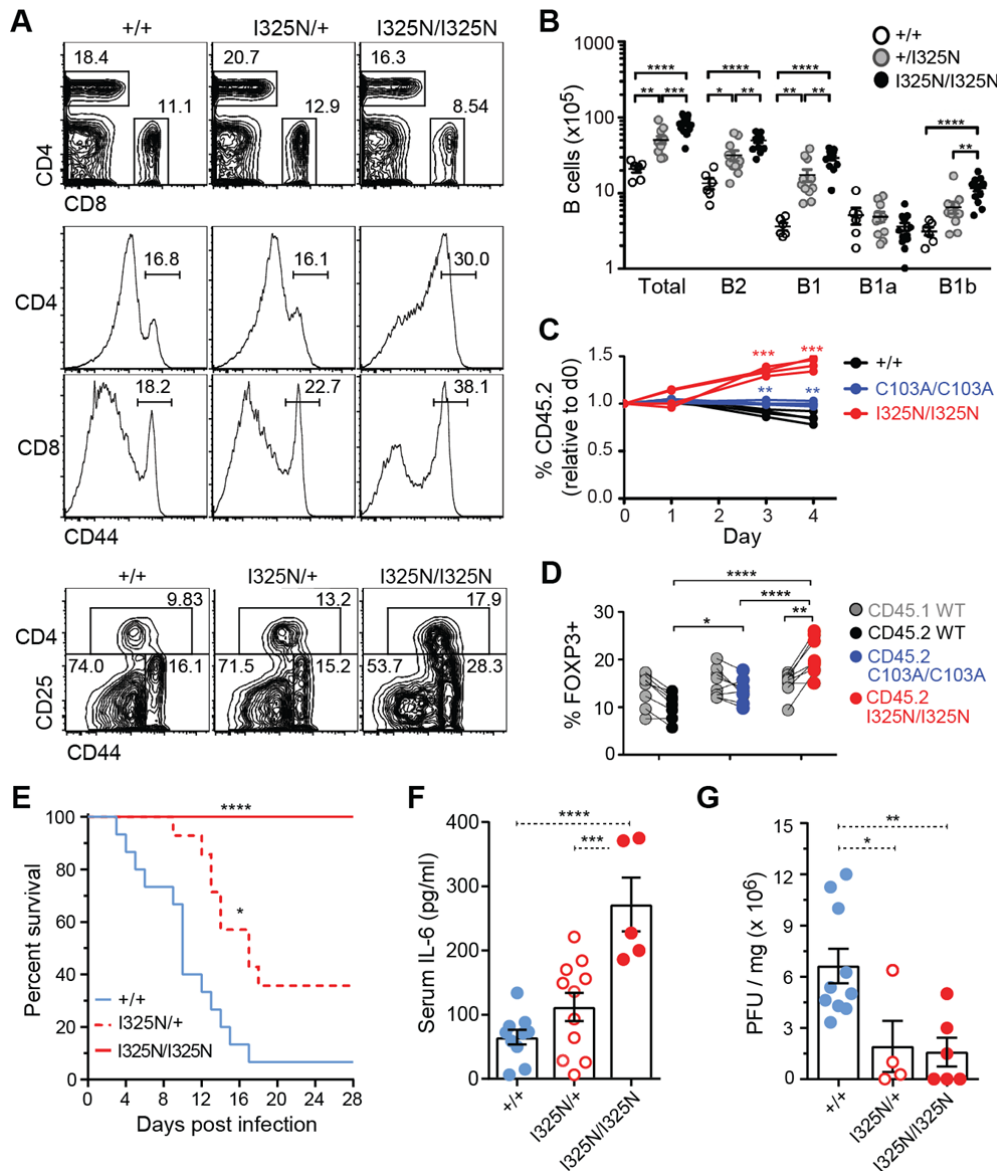
Fig. 2. I325N OTU variant confers heightened immunity in mice. (A) Representative flow cytometric analysis of splenocytes, showing percentage of CD4$^+$ or CD8$^+$ T cells, and percentage CD44^{hi} activated/memory cells within these subsets or percentage CD25$^+$ CD44^{int} regulatory T- cells or CD25$^-$ CD44^{high} effector/memory T cells among CD4$^+$ cells. **(B)** Numbers of indicated B cells in peritoneum of individual *Tnfaip3* mice (circles). **(C, D)** Wild-type CD45.1$^+$ mice transplanted with equal mixtures of congenic bone marrow from *Tnfaip3*$^{+/+}$ CD45.1$^+$ donors and CD45.2$^+$ donors of *Tnfaip3*$^{I325N/I325N}$, *Tnfaip3*$^{C103A/C103A}$ or *Tnfaip3*$^{+/+}$ genotypes. (C) Splenocytes from chimeras cultured with 0.1 μg/ml LPS for 0-4 days, and the frequency of CD45.2$^+$ cells of the indicated *Tnfaip3* genotypes was measured among B cells from individual chimeras (lines), expressed relative to their frequency on day 0. (D) Pairwise comparison of frequency of FOXP3$^+$ cells amongst CD45.2$^+$ and CD45.1$^+$ CD4$^+$ splenocytes from the same chimera. **(E-G)** Female *Tnfaip3*$^{+/+}$ (*n*=15), *Tnfaip3*$^{I325N/+}$ (*n*=14) or *Tnfaip*3$^{I325N/I325N}$ (*n*=10) C57BL/6 mice were injected with Coxsackie B4 virus strain E2 on day 0. (E) Kaplan-Meier survival data (Log-rank test). (F) Plasma IL-6 and (G) virus titers (plaque forming units, PFU) per mg of pancreas on day 3. Error bars represent

16

605   SEM and one-way ANOVA used for significance analysis unless otherwise stated, *$P < 0.05$;
606   **$P < 0.01$; ***$P < 0.001$; ****$P < 0.0001$.
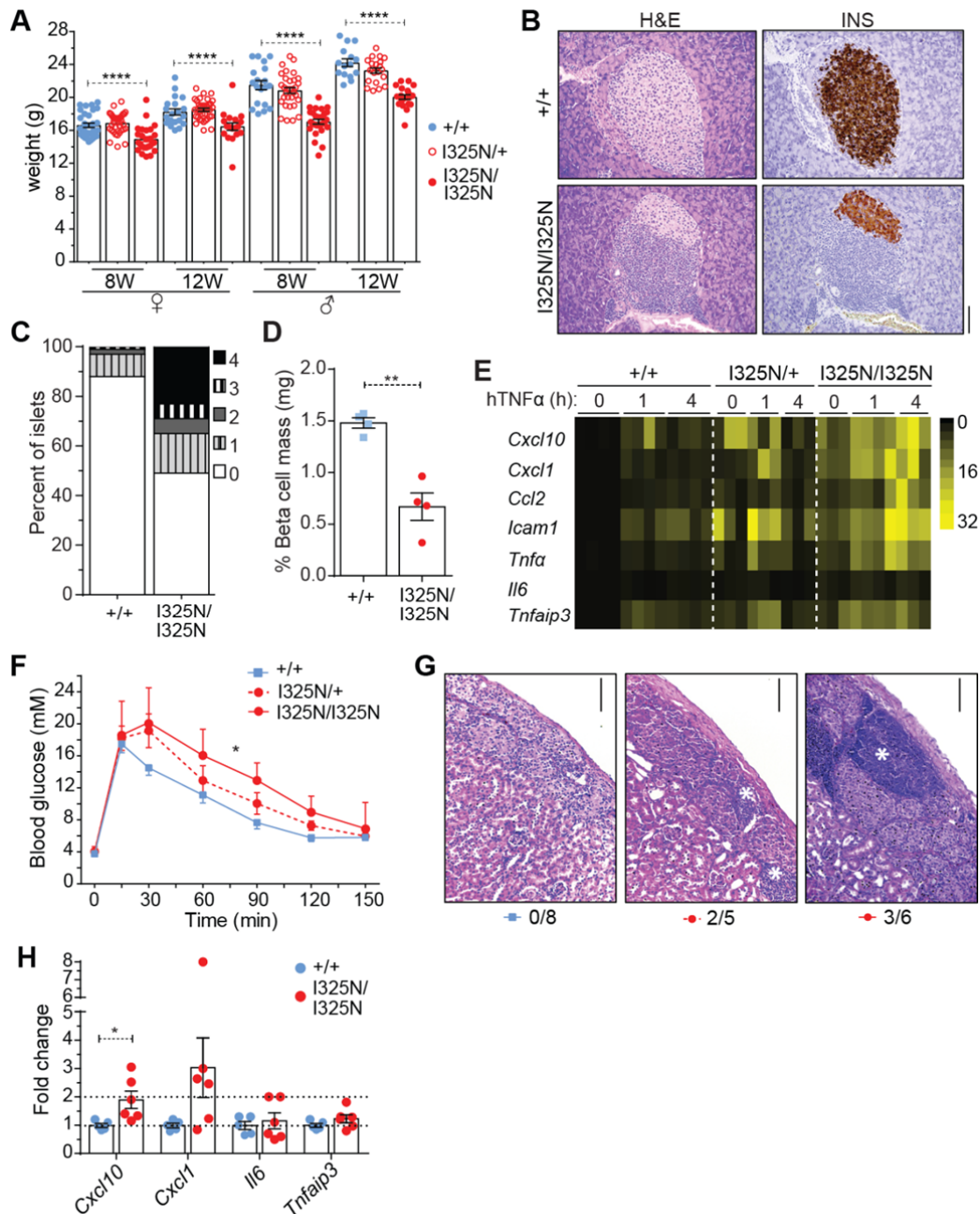
Fig. 3. Subclinical inflammatory and metabolic consequences of the I325N variant. (A) Body weights of *Tnfaip3*^{+/+}, *Tnfaip3*[I325N/+], *Tnfaip3*[I325N/I325N] mice of the indicated age and sex. Statistical analysis by unpaired one-way ANOVA: ****$P < 0.0001$. **(B)** Hematoxylin and eosin (H&E) and insulin (INS) stained pancreas sections (scale = 100 μm) with **(C)** cumulative insulitis scores (4 represents >75% islet mononuclear cell infiltration, and 0 an absence of infiltrating cells) and **(D)** calculated beta cell mass for *Tnfaip3*^{+/+} and *Tnfaip3*[I325N/I325N] mice. **(E)** Expression of TNFα-induced genes in islets from *Tnfaip3*^{+/+}, *Tnfaip3*[I325N/+], *Tnfaip3*[I325N/I325N] mice. Data represents 3 independent islet preparations with 3-4 biological replicates. **(F)** Glucose tolerance test in diabetic wild-type mice transplanted with *Tnfaip3*^{+/+}, *Tnfaip3*[I325N/+] or *Tnfaip3*[I325N/I325N] islets, N>8 mice per group. **(G)** H&E sections of islet grafts at post-operative day 30 (scale = 50 μm) with the fraction of grafts exhibiting immune infiltrate shown below. **(H)** Islet grafts isolated on post-operative day 10 were

620   analysed for indicated mRNAs by RT-qPCR. P values represent Student's t-test unless
621   otherwise stated, $*P < 0.05$; $**P < 0.01$; $****P < 0.0001$.
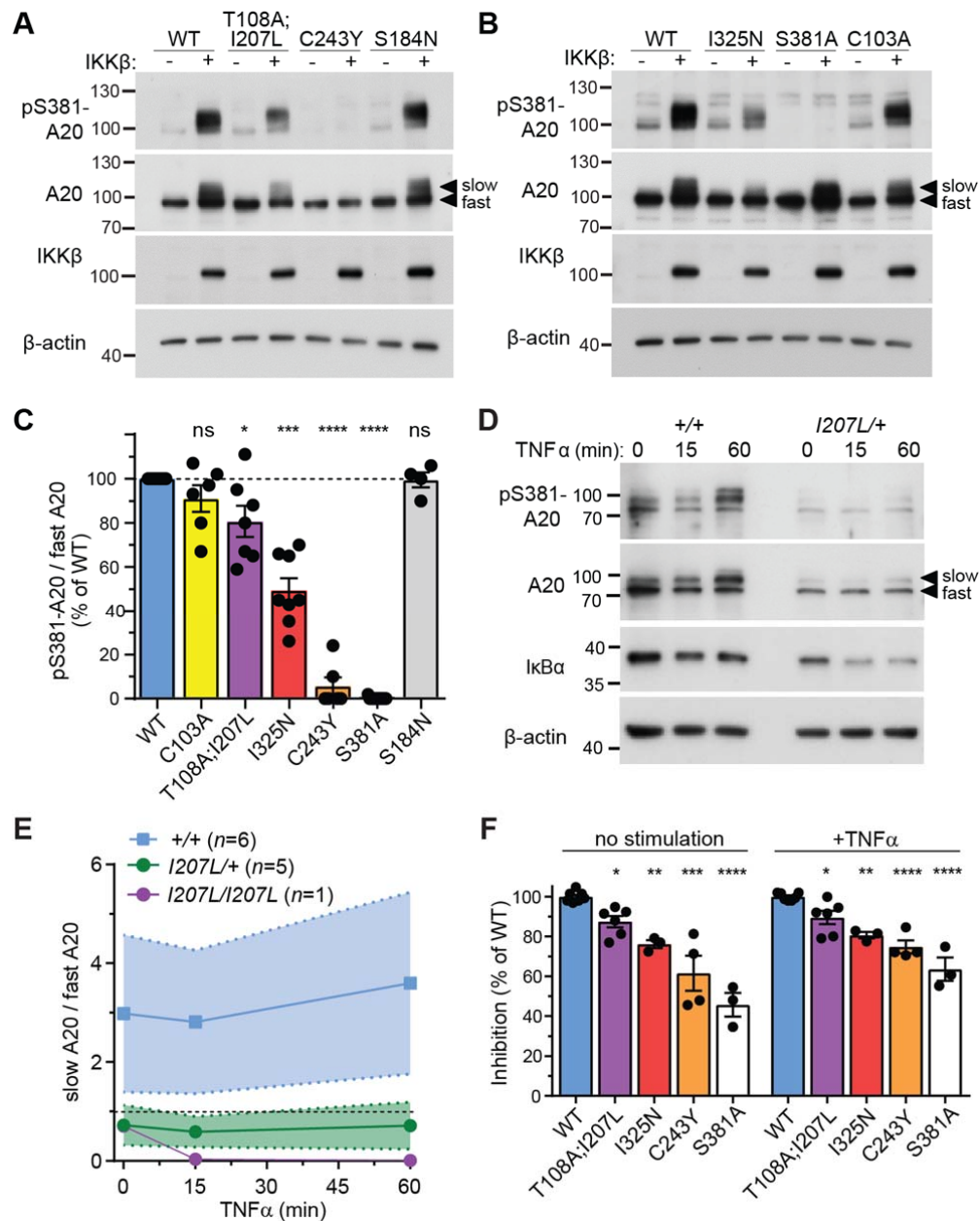
Fig. 4. OTU domain variants decrease A20 phosphorylation and NF-κB inhibition. (A-C) Representative western blot of lysates from βTC3 mouse insulinoma cells transfected with vectors encoding wild-type (WT) A20 or the indicated A20 mutants, with or without co-transfected IKKβ, and probed with antibodies to phospho-Ser381 A20, total A20, IKKβ and β-actin. Molecular weight markers (kD) and slow- or fast-migrating A20 species are indicated. **(C)** Densitometric analysis from multiple independent experiments (dots) showing the ratio of pSer381-A20 to total fast migrating A20 in IKKβ-cotransfected cells, expressed relative to the ratio in cells with WT A20. **(D)** Representative western blot, probed with antibodies to the indicated proteins, of lysates from peripheral blood mononuclear cells from healthy donors with wild-type A20 or heterozygous for the Denisovan T108A;I207L haplotype, stimulated with TNFα for the indicated times. **(E)** Densitometric ratio of slow- to fast-migrating A20 species, showing mean and standard deviation from six normal donors, five T108A;I207L heterozygotes, and one T108A;I207L homozygote (Extended Data Fig.

20

636   14). **(F)** Inhibition of an NF-κB luciferase reporter in βTC3 cells by co-transfection of WT
637   A20 or the indicated A20 mutants, expressed relative to wild-type A20 (Extended Data Fig.
638   13). Statistical analysis in C and F by one-way ANOVA: ns, $P > 0.05$; *$P < 0.05$; **$P < 0.01$;
639   ***$P < 0.001$; ****$P < 0.0001$.

640

641
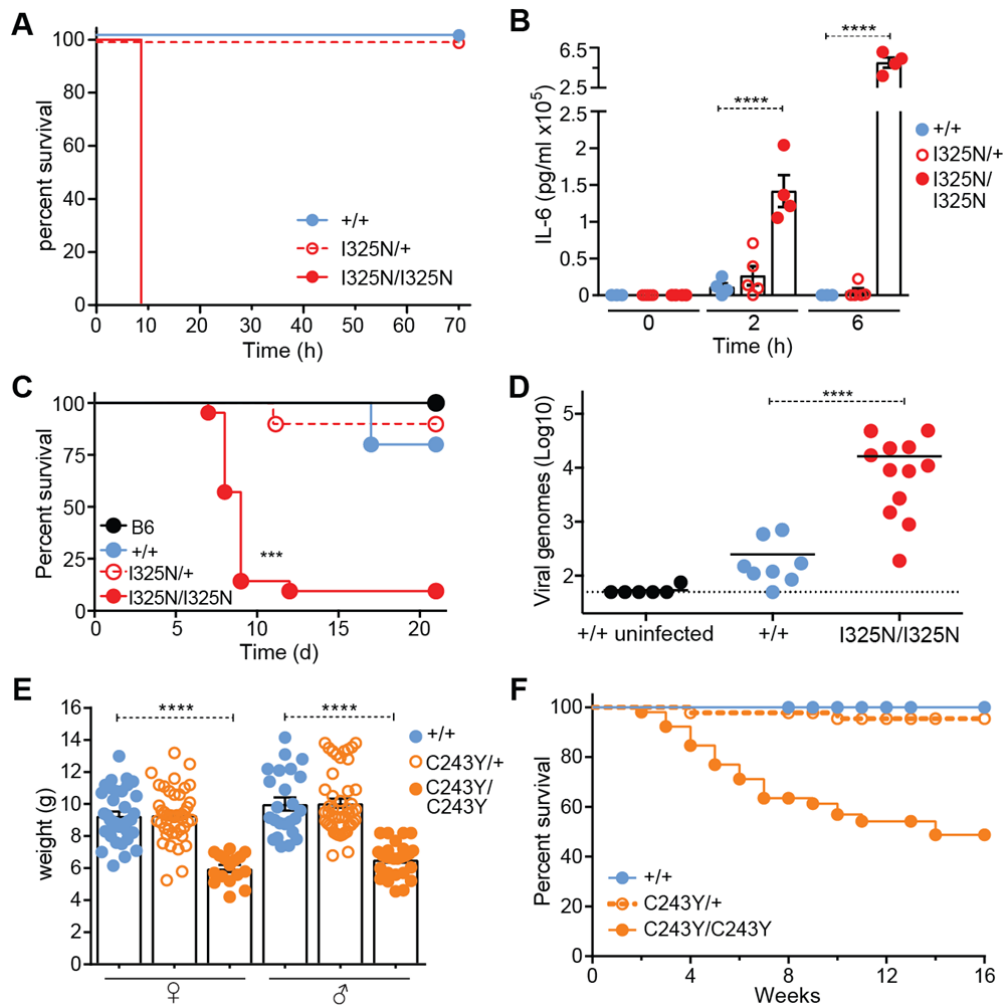
Fig. 5. Shift from beneficial to detrimental effects in response to environmental or genetic stressors. Kaplan-Meier survival curves **(A)** and serum IL-6 concentration **(B)** in mice of the indicated genotypes given 50 μg LPS by intraperitoneal injection at time=0. *N*=16-18 for each curve in (A). **(C)** Kaplan-Meier survival curves for sex-matched littermates of the indicated *Tnfaip3* genotypes and wild-type controls (B6) infected with Ectromelia virus. **(D)** Day 8 serum viral load assessed from mice in (C). **(E)** Weight of 3-week-old *Tnfaip3*[C243Y/C243Y] mice and heterozygous or wild-type littermates. **(F)** Survival of C243Y homozygous mice (*n*=52) compared to heterozygous (*n*=43) or wild-type littermates (*n*=41). Statistical analysis by Students *t*-test and one-way ANOVA: ***$P < 0.001$, ****$P < 0.0001$.

Materials and Methods

Human subjects

Patients and healthy family members were recruited via the Clinical Immunogenomics Research Consortium Australia and The Children's Hospital at Westmead, providing written informed consent under protocols approved by relevant human research ethics boards.

Genome sequencing

Parent-proband trio genomes were sequenced on the Illumina HiSeq X platform using DNA isolated from whole blood. Libraries were generated using either Illumina TruSeq PCR-free or TrueSeq Nano.

Raw reads were aligned to the hs37d5 reference using BWA-MEM v0.7.10-r789 (arXiv:1303.3997 [q-bio.GN]), and sorted and duplicate-marked with Novosort v1.03.01 (Novocraft Technologies). The GATK suite v3.3-0-g37228af [43] was used for local indel realignment and base quality score recalibration. gVCFs were generated with GATK HaplotypeCaller, joint-called as trios using GATK GenotypeGVCFs, and variants recalibrated using GATK Variant Quality Score Recalibrator (VQSR). Finally, VCF files were annotated with Variant Effect Predictor (VEP) v76[44] using the LoFTEE[45] and dbNSFP plugins.

Variants were packaged into databases using GEMINI (v0.18.3)[46] and imported into Seave[47]. All reported variants were manually inspected using IGV[48] to verify their authenticity and validated by Sanger Sequencing.

Population genetic analysis

TNFAIP3 genotypes were extracted from 279 publicly-available genomes from the Simons Genome Diversity Project samples[22], or exome data from 72 Martu indigenous Australians[32]. In addition, a collection of 514 individuals from across mainland and Island Southeast Asia, Papua New Guinea and Oceania was genotyped at 567,096 variants using the Affymetrix Axiom Genome-Wide Human Array, with 538,139 autosomal variants with <5% missing data kept for further analyses[30]. Weir and Cockerham's estimated F_{ST} values were calculated using VCFtools v0.1.14, and principal component analysis was performed using PLINK v1.9. Genotypes were phased and imputed using the Michigan Imputation Server v1.0.3 (http://imputationserver.sph.umich.edu), and compared to high-coverage Denisovan[27] and Altai Neanderthal[28] *TNFAIP3* haplotypes. Phred-scaled CADD scores[49] were calculated for all PASS variants across the extended Denisovan haplotype with gnomAD allele frequency <0.01.

PBMC isolation and manipulation

Human PBMCs were prepared using a Ficoll- Hypaque gradient and live count taken using 0.1 % trypan blue. Cells were resuspended at 10^6 cells/ml in sterile freezing medium (RPMI-1640, 10% DMSO, 50% FCS) in 1.5 ml Sarstedt cyrovials and stored in liquid nitrogen. Human PBMCs were thawed in a 37°C water bath and added drop wise to pre-warmed medium (RPMI-1640, 10% FCS, 100 U/ml P/S, 1% HEPES, 2 mM L-Glutamine, 2mM EDTA) and resuspended for culture at 37°C + 5% CO_2 for 1 h prior to stimulation with recombinant human TNFα (R&D Systems). Following stimulation, cells were pelleted and processed for immunoblotting or RT-qPCR, as described below.

Mice

The *Tnfaip3 Lasvegas* strain (*Tnfaip3*[I325N]) were generated by *N*-ethyl-*N*-nitrosourea (ENU) mutagenesis of C57BL/6 mice, and propagated by backcrossing to C57BL/6. The

701 strain was maintained as heterozygous breeding pairs so that WT littermates could be used
702 for controls. To generate *Tnfaip3*^{C243Y} mice, a guide RNA with the sequence 5′-
703 GGGATATCTGTAACACTCC-3′ was microinjected into C57BL/6 zygotes in combination
704 with Cas9 mRNA. Founder mice carrying the C243Y substitution were then crossed to
705 C57BL/6, and heterozygous offspring intercrossed to generate homozygous, heterozygous
706 and wild-type littermates for experimentation. Mouse lines were housed at the Australian
707 Phenomics Facility (Australian National University, Canberra, Australia), or at the Australian
708 BioResources Centre (ABR) (Moss Vale, NSW, Australia). *Tnfaip3*^{C103A} [18], 3A9 TCR
709 transgenic[50] and insHEL transgenic[51] mice have been described. Mice were genotyped for
710 transgenes and mutations by PCR and used 7–28 (typically 10-16) weeks after birth. For
711 TCR^{3A9} transgenic mouse experiments, mice were hemizygous for the 3A9 or insHEL
712 transgenes on the B10.BR and the B10.BR.SJL-*Ptprc*^{a} (CD45.1) backgrounds, and the
713 *Tnfaip3*^{I325N} mutation was backcrossed to B10.BR. To make chimeras, congenic B6.SJL-
714 *Ptprc*^{a} or B10.BR.SJL-*Ptprc*^{a} (CD45.1) mice were irradiated with two doses of 4.5 Gy 4 hrs
715 apart, and injected IV with mixtures of 1.8x10^6 bone marrow cells from B6 or B10.BR SJL-
716 *Ptprc*^{a} mice and 1.8x10^6 bone marrow cells from B6 (CD45.2) mutant or control mice, and
717 analyzed 8-14 weeks later. Animal studies were approved by the Garvan/St Vincent's or the
718 Australian National University Animal Ethics Committees. All procedures performed
719 complied with the Australian code of Practice for Care and Use of Animals for Scientific
720 Purposes.
721
722 <u>Coxsackievirus infection model and virus quantification</u>
723 Mice were intraperitoneally injected with normal saline (control) or 20 plaque forming
724 units (PFU) in 200 µl saline of the CVB4 E2 lab strain kindly provided by Prof. Malin
725 Flodström Tullberg (Karolinska Institutet, Solna, Sweden) grown in HeLa cells. Mice were
726 monitored daily and euthanized if they displayed gross signs of illness (e.g., ruffling,
727 hunching). The pancreas was harvested at indicated times for RT-qPCR and histopathology
728 analysis and viral titre determination. Serum was also collected by cardiac puncture for
729 measurement of IL-6 by ELISA (BD; OptEIA^{TM} Set Mouse IL-6), as per manufacturer's
730 instructions. Non-fasting blood glucose levels were measured at least twice-weekly using
731 Freestyle Lite Blood Glucose Test Strips (Abbott, Australia). Plaque assays were performed
732 to determine viral titres within the pancreas following infection. HeLa cells (0.6 x 10^6/well)
733 were seeded in 2 ml complete medium (RPMI with 10% FCS, 2mM L-Glutamine, 100 U/ml
734 Penicillin, 100 µg/ml Streptomycin and 100 µg/ml Normocon) in 6 well plates and incubated
735 over night at 37°C. Infections samples were collected in RPMI, homogenized in a Dounce
736 tissue grinder and passed through a 22 µm filter, before preparing tenfold serial dilutions.
737 HeLa cells, at 90% confluency, were washed with 1X PBS and 400 µl of infectious
738 homogenate added to each well and incubated for 60 min at 37°C under gentle rocking.
739 Infectious media was removed and 3 ml of agar mix (2x 1.8% agar, 2x MEM containing 10%
740 FCS) was added to each well before incubating at 37°C for 3 days. Cells were then fixed with
741 Carnoys reagent for 60 min and subsequently stained with 0.5% Crystal violet for 60 s. Wells
742 were extensively washed with H$_2$O and plaques counted.
743
744 <u>Ectromelia virus model</u>
745 Mice were inoculated subcutaneously with 10^3 PFU Ectromelia virus (Moscow strain;
746 ATCC #VR-1374) in the flank of the left hind limb between the regio tarsi and regio pedis
747 under avertin anesthesia. Clinical scores were recorded daily, and animals weighed on days 0,
748 5 and every 2 days thereafter until day 21, and bled on days -1 and 8 to measure viral load.
749 Animals with a significant clinical score or 25% decrease of starting weight were euthanized
750 and considered dead the following day. Viral load was measured in blood by qPCR for

751 *ECTV-Mos-156* viral genomes and in organs by viral plaque assay as $\log_{10}$ PFU/gram
752 tissue[52].
753
754 Macrophage cultures
755   Bone marrow from femurs and tibiae was cultured 7 days in complete RPMI1640
756 medium with 10% fetal bovine serum, 100U/ml penicillin, 100μg/ml streptomycin, 2mM L-
757 glutamine (Life Technologies) and 50ng/ml recombinant human Macrophage colony-
758 stimulating factor (Peprotech). Cells were placed into 6-well plates for stimulation with
759 10ng/ml Salmonella Minnesota R595 (Re) ultra-pure LPS (List Biological) for different time-
760 points. RNA was extracted by TRIzol (Life Technologies), reverse transcribed to cDNA with
761 SuperScriptII (Life Technologies), *Cxcl1* and *Cxcl11* levels were measured using the Taqman
762 assay (Applied Biosystems). RNA levels relative to *Ef1a* were calculated with the delta Ct
763 values. Conditionally *Hoxb8*-immortalized bone-marrow progenitor cells were generated as
764 described[53].
765
766 LPS sepsis model
767   A low dose of 50μg LPS was administered by intraperitoneal injection. Mice were
768 monitored every 1 h for 10 h and sacrificed if ethical end-point reached. Monitoring was
769 conducted using body conditioning score and Grimace Scale (NC3Rs [National Centre for the
770 Replacement Refinement & Reduction of Animals in Research) approved by the Garvan/St
771 Vincent's Animal Ethics Committee. Monitoring continued twice daily for 7 days in
772 surviving mice, were weights and blood glucose levels were also measured. Serum was
773 collected by tail-tipping before LPS injection and 2 and 4 hours following injection for IL6
774 determination by ELISA (BD; OptEIA[TM] Set Mouse IL-6), as per manufactures instructions.
775
776 Immunohistochemistry and beta cell area determination
777   Tissues were fixed in 10 % neutral buffered formalin (Sigma-Aldrich), paraffin
778 embedded and parallel sections (5 μm) prepared. Sections were stained with hematoxylin and
779 eosin (H&E; Sigma-Aldrich) and for pancreatic tissue parallel sections stained for insulin
780 (purified rabbit anti-mouse insulin polyclonal antibody; 4590; Cell Signaling Technology).
781 Visualization of bound anti-insulin antibody was achieved using HRP-labelled polymer-
782 conjugated goat anti-rabbit IgG (Dako EnVision+ System), followed by counterstain with
783 hematoxylin. For pancreatic beta cell mass determination consecutive pancreatic serial
784 sections at 200 μm intervals were stained for insulin and beta cell area quantified from total
785 area taken by insulin positive cells compared to non-positive tissue (ImageJ). Beta cell mass
786 (mg) was calculated by multiplying relative insulin-positive area by the mass of the isolated
787 pancreas before fixation. Images were captured using a Leica DM 4000 or Leica DM 6000
788 Power Mosaic microscope (Leica Microsystems).
789
790 Metabolic studies
791   Blood glucose levels (BGL) were determined using a FreeStyle Lite® glucometer and
792 blood glucose test strips (Abbott Diabetes Care) via tail tipping. Measurements were taken
793 from 8 and 12 week old male or female non-fasted mice. Intraperitoneal glucose tolerance
794 tests (IP-GTT) were conducted following an overnight fast (16 h) with access to water. The
795 following day mice were weighed and fasting blood glucose measurements taken.
796 Subsequently, mice were injected (IP) with 20% dextrose w/v (Sigma Aldrich) to a final
797 concentration of 2 g glucose per kg body weight (2g/kg). Blood glucose levels were
798 measured from the tail vein at 15, 30, 60 and 120 min post-glucose administration.
799 Intravenous (IV) GTT was conducted in a similar manner; however, glucose (1 g/kg) was
800 administered intravenously into the tail vein and blood glucose measurements taken at 0, 5,

801   10, 15, 20, 30, and 60 min post-injection. During the IV-GTT blood samples were also taken

802   for the determination of insulin content via ELISA, conducted as per manufactures

803   instructions (Cayman Chemical). Glucose-stimulated insulin secretion assay (GSIS) was

804   performed for islets *ex vivo* as descried[54].

805

806   <u>Islet isolation, transplantation, and *in vitro* studies</u>

807   Islets were isolated as previously described[55], and counted for islet transplantation or *in*

808   *vitro* experiments using a Leica MZ9.5 stereomicroscope. Islets were transplanted under the

809   kidney capsule of diabetic B6 littermates as described[56]. Diabetes was induced by IP

810   injection of 180 mg/kg streptozotocin (Sigma-Aldrich) dissolved in 0.1 M citrate buffer (pH

811   4.2) at a concentration of 20 mg/ml. Diabetes was determined as [blood glucose] $\geq$16 mM on

812   two consecutive days measured by FreeStyle Lite® glucometer and Abbott Diabetes Care test

813   strips following tail tipping. Islet grafts were retrieved from recipients at indicated time points

814   post-transplantation for analysis of islet morphology, function, or degree of lymphocytic

815   infiltration by histology or gene expression by RT-qPCR. Gene expression in islet grafts was

816   calculated using the average WT ΔCt value. Islets to be used for *in vitro* studies were cultured

817   overnight in islet overnight culture media (RPMI-1640, 20% FCS, 100 U/ml P/S, 2 mM L-

818   Glutamine) at 37°C + 5% CO_2.

819

820   <u>Flow cytometry</u>

821   Flow cytometric staining was performed as described in[57,58]. Antibodies against the

822   following surface antigens were: CD4 (RM4-5), CD8 (53-6.7), CD21 (7G6), CD23 (B3B4),

823   CD25 (PC61.5), CD44 (IM7), CD69 (H1.2F3), CD93 (AA4.1), CD45.2 (104), B220 (RA3-

824   6B2), IgM (II/41), IgD (11-26). Splenocytes were labeled with CFSE (Invitrogen) and

825   cultured in RPMI1640 supplemented with 10% FCS, 2 mM L-glutamine, 55 µM 2-

826   mercaptoethanol, and penicillin/streptomycin. B cells were stimulated with: F(ab')$_2$ goat anti-

827   mouse IgM (10 µg/ml , Jackson Immunoresearch Laboratories), LPS from *E. coli* 055:B5

828   (10, 1, 0.1 µg/ml, SIGMA), anti-CD40 (10 µg/ml FGK4.5, BioXCell). When analysing 3A9

829   TCR transgenic cells single cell suspensions from thymus, spleen or pancreatic lymph node

830   were incubated for 30 min at 4° C in culture supernatant from the 1G12 hybridoma (specific

831   for TCR[3A9]). Then, cells were pelleted by centrifugation and incubated for 30 min at 4° C in

832   FACS buffer containing assortments of fluorochrome- or biotin-conjugated monoclonal

833   antibodies against cell surface proteins. After washing in FACS buffer, cells were fixed and

834   permeabilised using the eBioscience Foxp3 staining buffers, then incubated with antibodies

835   specific for intracellular proteins and Brilliant Violet 605-streptavidin conjugate (BioLegend)

836   to detect biotin-conjugated antibodies. Antibodies were purchased from BD, eBioscience or

837   BioLegend. Data were acquired with LSR II flow cytometers (BD) and analyzed using

838   FlowJo software (Tree Star).

839

840   <u>CyTOF:</u>

841   Unstimulated spleen cells from four wild-type and four I325N-homozygous mutant mice

842   were individually labeled with mass-barcodes, mixed, permeabilized and stained with mass-

843   labeled antibodies to a panel of cell surface markers and intracellular proteins including IκBα,

844   and analyzed by CYTOF mass spectrometry[59,60]. Spanning-tree Progression Analysis of

845   Density-normalized Events (SPADE)[61] analysis was used to resolve leukocyte lineages and

846   subsets, and the relative intensity of IκBα in each subset compared between mutant and wild-

847   type cell counterparts.

848

849

850

851 <u>Real Time quantitative PCR (RT-qPCR)</u>
852   Mouse islets were isolated and placed into 12-well non-tissue culture-treated plates (150-
853 200 islets/well; Fisher Scientific). Following an overnight culture islets were treated with
854 200 U/ml recombinant human (h) TNFα (R&D Systems) for 1, 4, or 24 h. Total RNA was
855 extracted using the RNeasy Plus Mini Kit (Qiagen) and reverse transcribed using Quantitect
856 Reverse Transcription Kit (Qiagen). Primers were designed using Primer3 software[62] with
857 sequences obtained from GenBank and synthesized by Sigma Aldrich (Table 3, 4). PCR
858 reactions were performed on the LightCycler®480 Real Time PCR System (Roche) using the
859 FastStart SYBR Green Master Mix (Roche). Cyclophilin (CPH) was used as the
860 housekeeping gene and data analyzed using the $2^{\Delta\Delta CT}$ method. Initial denaturation was
861 performed at 95° C for 10 sec, followed by a three-step cycle consisting of 95° C for 15 sec
862 (4.8° C/s, denaturation), 63° C for 30 sec (2.5° C/sec, annealing), and 72° C for 30 sec (4.8°
863 C/s, elongation). A melt-curve was performed after finalization of 45 cycles at 95° C for 2
864 min, 40° C for 3 min and gradual increase to 95° C with 25 acquisitions/° C. Expression
865 differences were visualized using GraphPad or BAR Heatmapper plus tool.
866
867 <u>Immunoblot analysis and immunoprecipitation</u>
868   Primary islets were lysed in islet lysis buffer (50 mM Tris-HCL pH7.5, 1% Triton X,
869 0.27 M sucrose, 1 mM EDTA, 0.1 mM EGTA, 1 mM Na_3VO_4, 50 mM NaF, 5 mM
870 Na4P2O7, 0.1% β-mercaptoethanol; supplemented with EDTA-free protease inhibitor
871 [Roche]), βTC$_3$ cells were lysed with radioimmunoprecipitation (RIPA) buffer with SDS,
872 following relevant treatment with or without 200 U/ml of recombinant human (h) or mouse
873 (m) TNFα (R&D Systems). Protein concentration was measured using the Bradford assay
874 (Bio-Rad) and total protein (20-25 µg) resolved on a 7 - 10% SDS PAGE gel and then
875 transferred to a nitrocellulose membrane, Immobilon-P® (Merck Millipore). Membranes
876 were incubated with anti-IκBα (9242), anti-phospho-IκBα (9256), anti-JNK (9252), anti-
877 phospho-JNK (9255), anti-IκKα (2682), anti-phospho-IκKα/β (16A6; 2697), anti-NIK
878 (4994), anti-NF-κB2 p100/p52 (4882), anti-RelB (C1E4, 4922) (Cell Signaling Technology);
879 anti-beta-actin (AC15) (Sigma-Aldrich); or anti-S381-A20 (a kind gift by Professor Derek W.
880 Abbott[19]) followed by horseradish peroxidase (HRP)-labeled secondary antibody goat-anti-
881 mouse IgG Fc (Pierce Antibodies) or donkey-anti-rabbit IgG (GE Life Sciences). HRP
882 conjugates bound to antigen were detected and visualized by using an ECL detection kit (GE
883 Life Sciences).
884   Immunoprecipitation was conducted in thymocytes, which were lysed at 4°C in
885 immunoprecipitation buffer (0.025M Tris, 0.15M NaCl, 0.001M EDTA, 1% NP-40, 1%
886 Triton X 100, 5% glycerol) containing Complete® protease inhibitor and Phosphostop®
887 phosphatase inhibitors (Roche). Immunoprecipitation was then conducted by first preclearing
888 lysates with protein A/G-Sephrose (Thermo Fisher Scientific) for 1 h and then incubated with
889 anti-TNFR1 (ab7365) cross-linked beads or anti-A20 (59A426) antibody (Abcam) for 2 h at
890 4°C. Following incubation with only antibody 25 µl of protein A/G beads were added and
891 incubated at 4° C on a roller overnight. Beads were washed 4 X with lysis buffer and then
892 eluted using low pH amide buffer for cross-linked beads or 30 µl of Laemmli reducing gel-
893 loading sample buffer for non-cross linked beads. Samples were vortexed, heated to 100° C
894 for 5 min, cooled on ice for 10 min, and then loaded onto a 8 or 10% agarose gel for
895 immunoblotting for anti-A20 (56305/D13H3), anti-IκBα (9242), anti-IκKβ (2684), anti-JNK
896 (9252), anti-TAK1 (52065), anti-phospho-IκBα (9256), anti-phospho-JNK (9255), anti-
897 phospho-TAK1 (4536/90C7), anti-TNFR1 (3736C25C1) (Cell Signaling Technology), anti-
898 RIP1 (H-207) (Santa Cruz), anti-RIP1 (610458) (BD bioscience), anti-TAK1 (491840) (R&D
899 systems), or anti-beta-actin (AC15) (Sigma-Aldrich). For B cell stimulation, splenic B cells
900 purified by MACS with CD43 depletion were stimulated with anti-IgM F(ab')2 or LPS for

901   the indicated times. Cells were lysed with TNE buffer (1% Nonidet P-40, 20 mM Tris-HCl,

902   pH 8.0, 150 mM NaCl, 0.1 mM sodium orthovanadate, and complete protease inhibitor

903   [Roche]). The following antibodies were used: anti-IκBα (9242), anti-TNFAIP3

904   (5630/D13H3) (Cell Signaling Technology), anti-A20 (A-12), anti-ubiquitin (P4D1) (Santa

905   Cruz) and anti-beta-actin (AC-15) (Sigma-Aldrich).

906

907   *In vitro* reporter transfection studies

908   Reporter assays were carried out as described previously[63,64]. NF-κB activity

909   experiments were conducted using βTC_3 cells transfected with 0.3 μg of the NF-κB.Luc

910   reporter (Promega) and 0.25 μg CMV.β-galactosidase (a kind gift from Beth Israel Harvard

911   Medical School, Boston, MA). pcDNA vectors encoding human WT or variant A20

912   constructs or the empty pcDNA3.1 reporter were then added (0.3 μg), and each well topped

913   with 0.15 pcDNA3.1 to make 1 μg total DNA. Transfection was conducted using

914   Lipofectamine 2000 (Invitrogen). Following transfection cells were stimulated with 200 U/ml

915   of recombinant human (h) TNFα (R&D Systems). Luciferase activity was assayed in cell

916   lysates harvested 8 h post-stimulation, using a luciferase assay kit (Promega). Results were

917   normalized to β-galactosidase activity (Galactostar) to give relative luciferase activity.

918   Expression plasmids and reporters were obtained and maintained as described previously[63,64].

919

920   Ubiquitination assays

921   Wildtype A20, A20[I325N] or A20[C103A] OTU domain protein (1 μg) purified from *E. coli*

922   was added to 2 μg of K48-ubiquitin chains of mixed chain length (Ub_2-Ub_7) or to purified

923   tetra-ubiquitin (Ub_4) (#UC-230, UC-210, Boston Biochem). A20 OTU domains added to

924   mixed-length K48-ubiquitin chains were incubated in 100 μl of deubiquitin buffer (50 mM

925   HEPES pH 8.0, 0.01% Brij-35, 3mM DTT) at 37° C with agitation at 400 rpm for 60 or 150

926   min in a benchtop incubator shaker. A20 OTU domains added to K48-tetra-ubiquitin chains

927   were incubated in 100 μl of deubiquitin buffer (25 mM HEPES pH 8.0, 5 mM DTT, 5 mM

928   $MgCl_2$). At the indicated times, 20 μl of reaction mixture was collected and the enzymatic

929   reaction stopped by addition of SDS sample buffer. Recombinant Flag-tagged full length

930   A20^{+/+} or A20[I325N], was expressed in HEK-293T cells and purified as described

931   previously[14,17]. Full-length A20 deubiquitination reactions were performed using 100ng

932   recombinant A20, 500 ng of the indicated ubiquitin chain and DUB reaction buffer with or

933   without phosphatase inhibitor cocktail and were incubated for the indicated times at 37° C

934   with agitation at 1,000 rpm. Following incubation samples were placed on ice and 20 μl

935   collected and added to SDS sample buffer to stop the reaction. Full-length ubiquitin ligase

936   assay was performed as previously described[14]. Samples were subjected to 1D SDS-PAGE

937   and immunoblotted for ubiquitin (clone P4D1; Santa Cruz or Cell Signaling Technology) or

938   A20 (clone 59A426; Abcam or A-12; Santa Cruz), as described above.

939

940   OTU protein preparation and crystallisation

941   The N-terminal OTU domains of human and mouse A20 (human WT and I325N,

942   residues 1-366; mouse WT and C103A, 1-360) were cloned into vector pGEX-6P-1 (GE

943   Healthcare), facilitating bacterial expression as a GST-fusion. Sequences were confirmed by

944   Sanger sequencing. Expression was performed in *E. coli* strain BL21 (DE3) Gold, where

945   cells were induced at an OD600 of 0.5 with 0.2 mM IPTG, followed by incubation at 20° C

946   overnight in LB medium. Cells were harvested by centrifugation, lysed by three cycles of

947   freeze-thaw and one cycle of pressure shock (human WT and I325N) or by sonication alone

948   (mouse WT and C103A). The GST-fusions was captured from the cleared lysate by passage

949   over GSH-Sepharose CL4B resin (GE). For purification of human WT and I325N, the resin

950   was washed (50 mM Tris (pH 8.8) 200 mM NaCl, 5 mM DTT, 1 mM EDTA), then the A20

951   component released by overnight incubation (4° C) with PreScission protease. Eluted A20
952   was stabilized by incubation with iodoacetamide (Sigma; 30 mM, 30 min at RT). The
953   reaction was terminated by addition of an equivalent amount of β-mercaptoethanol. For
954   purification of mouse WT and C103A protein, purified GST-OTU fusion protein was eluted
955   (50 mM Tris-HCl [pH 8.0], 200 mM NaCl, 5 mM DTT, 10 mM glutathione) from the column
956   and the A20 OTU component was released by overnight incubation (4° C) with PreScission
957   protease. The cleavage products were subject to anion-exchange chromatography (HiTrap Q
958   FF; GE) where the OTU domain eluted as a single peak between 5 and 500 mM NaCl, 25
959   mM Tris-HCl pH 7.5. All proteins were then concentrated and subject to gel filtration
960   chromatography (ÄKTA S200 26/60, buffers as described above).
961   Crystals of both the $A20^{I325N}$ variant (long triangular rods) and wild-type A20 (long rods)
962   OTU domains, grown under the same conditions; equal volumes of protein (2.7 mg/mL) and
963   well solution (50 mM $CaCl_2$, 100 mM MES (pH 6.0), 5% PEG1500) were combined in a
964   hanging drop setup. Crystals grew over several weeks at RT. Partial cryoprotection was
965   achieved by briefly (1-5 seconds) swimming crystals in a solution comprising equal volumes
966   of mother liquor and well solution doped with glycerol (25% v/v final) prior to being plunge
967   vitrified in liquid N_2. For the mouse wild-type A20, crystallization was achieved by vapor-
968   diffusion in hanging-drops at a protein concentration of 8 mg/mL in 1.8 - 2.4 M NaCl, 0.1 M
969   MES [pH 6-6.7]. Crystals were soaked in mother liquor containing 30% ethylene glycol for
970   one minute and immediately vitrified in a nitrogen cryo-stream.
971
972   <u>Crystallographic data reduction and model refinement</u>
973   Diffraction data using light of wavelength 0.9537 Å was collected at 100 K at beamline
974   MX2 at the Australian Synchrotron. Data were indexed and integrated with MOSFLM[65]. The
975   spacegroups were scrutinized with POINTLESS, and the data scaled with AIMLESS[66,67], or
976   SCALA[68] accessed via the CCP4i software interface[69]. Although grown under essentially the
977   same conditions, the human WT and I325N mutant A20 proteins crystallized in different
978   space groups. These data were highly anisotropic, resulting in poor completeness, low
979   multiplicity, and noisy electron density maps. In the case of the mouse OTU crystal, there
980   was significant thermal diffuse scattering. See Table 5 for data reduction and refinement
981   statistics.
982   Structures were solved by molecular replacement using PHASER[70]. The search model
983   was the A-chain of PDB entry 3DKB, but stripped of surface loops that displayed
984   conformational variability in other PDB entries (2VFJ and 3ZJD). In the case of the human
985   I325N data the structure was originally solved in the space-group $P3_12$ with 4 molecules in
986   the asymmetric unit. However, crystal packing and residual unaccounted-for electron density
987   suggested more molecules might be present. The structure was subsequently solved in the
988   lower symmetry $P3_1$ space group, with 6 molecules in the asymmetric unit, sensible packing
989   and no unaccounted-for density. The human wild-type A20 structure, solved as a control for
990   the iodoactamide alkylation, also has 6 molecules (three dimers) in a different asymmetric
991   unit and space group. The mouse OTU structure was indexed and refined in the $P3_2$ space
992   group, with a dimer in the asymmetric unit. Restrained B-factor refinement, using local non-
993   crystallographic symmetry (NCS) restraints, was performed with REFMAC5[71]. For the
994   mouse A20 OTU structure TLS and restrained refinement was carried out using
995   phenix.refine[72]. Between rounds of refinement, electron density maps and composite OMIT
996   maps[73] and their fit to the model were examined using COOT[74]. Amino acid side chains were
997   added/subtracted if suggested by difference map electron density. The active-site cysteine
998   (C103) was clearly identified through inspection of mFo-Dfc difference maps as the only
999   cysteine residue alkylated by the iodoacetamide treatment in both human structures (PDB
1000   residue descriptor YCM). All 6 molecules refined in each structure are highly similar in fold,

1001   both to themselves, and compared with each other. All molecules form dimers with
1002   neighboring molecules, as observed in other crystal structures. Structure validation was
1003   performed using the MOLPROBITY web server[75]. The final human I325N, human WT, and
1004   mouse WT structures contain Ramachandran favored/outlier components of 88.64/0.00%,
1005   88.13/2.87 %, and 82.13/7.87 %, respectively.

1006

1007   <u>Measurement of OTU domain thermal stability</u>
1008   Purified A20 OTU domains (0.4 mg.mL^{-1}) were exchanged into 100 mM NaCl, 5 mM
1009   dl-dithiothreitol, 20 mM Na_2HPO_4 (pH 7.5). Circular dichroism data were collected with a
1010   Chirascan circular dichroism spectrometer (Applied Photophysics, UK) in a 1 mm cuvette.
1011   The protein was heated from 20°C to 90°C at a rate of 1°C min^{-1} while ellipticity was
1012   monitored at 220 nm. The thermally induced unfolding of A20 OTU domains was not
1013   reversible. The unfolding of the A20 OTU domains was described by a two-state model[76]
1014   (**Equation 1**).

1015

1016   **Equation 1**

$$y_{obs} = \frac{y_n + m_n T + (y_u + m_u T)\exp\left(\frac{\Delta H_{vH}}{R}\left(\frac{1}{T} - \frac{1}{T_{trs}}\right)\right)}{1 + \exp\left(\frac{\Delta H_{vH}}{R}\left(\frac{1}{T} - \frac{1}{T_{trs}}\right)\right)}$$

1017

1018   Where y_{obs} is the observed elipticity, y_n and y_u are the elipticity values observed for the
1019   native and unfolded states, respectively. The m_n and m_u values are the linear temperature
1020   dependencies of y_n and y_u. ΔH_{vH} is the apparent van't Hoff enthalpy, R is the universal gas
1021   constant, and T_{trs} is the temperature at which the population of unfolded protein is 50%.
1022   Curves were fit by non-linear regression using GraphPad Prism v6 (GraphPad Software).

1023

1024   <u>Statistical methods</u>
1025   Results are expressed as mean +/- standard error mean (SEM). Statistical analysis was
1026   performed using the Student's *t*-test or ANOVA were indicated.
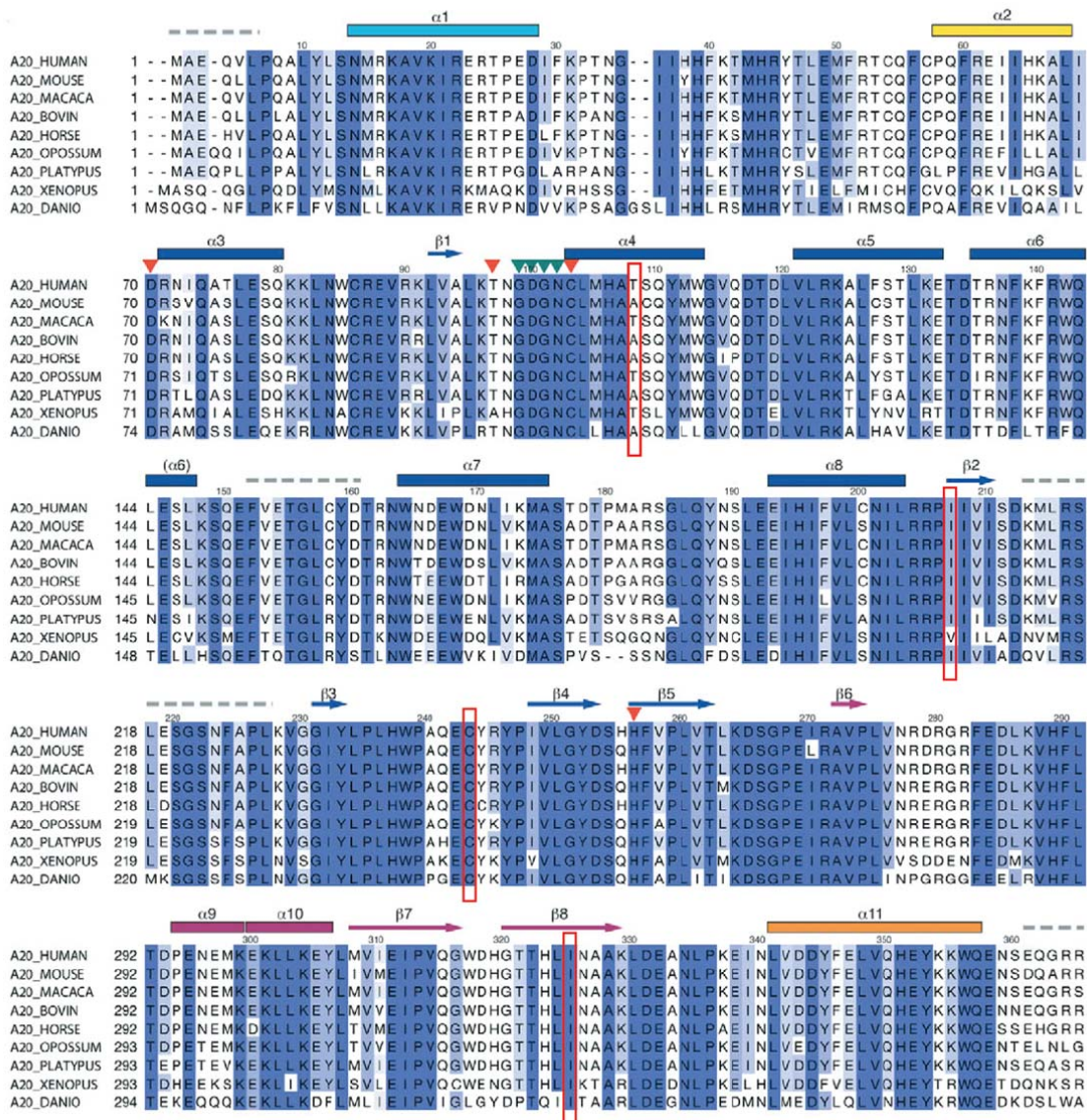
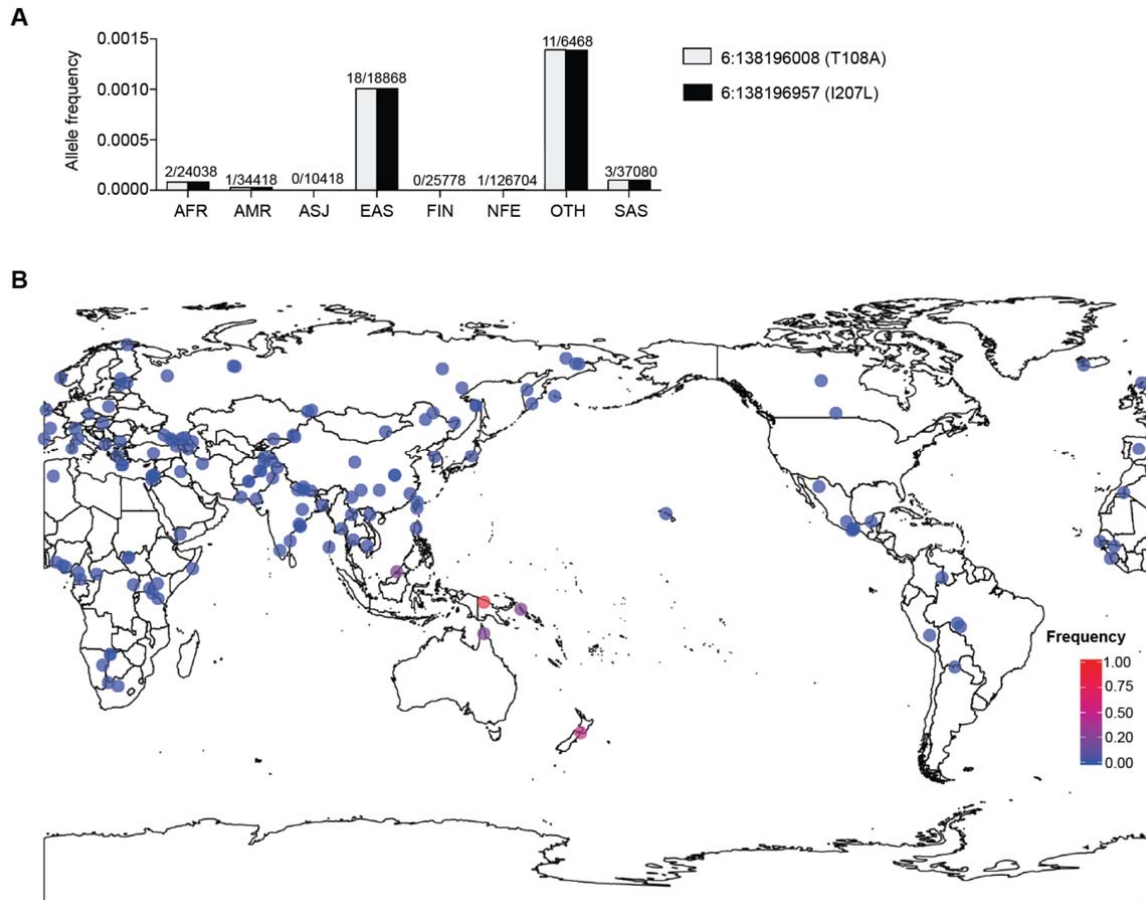1027 **Supplementary Text**
1028
1029 Extended Figure 3 legend:

1030 **Fig.3. Subclinical inflammatory and metabolic consequences of the I325N variant. (A)**
1031 Body weights of 8 and 12 week old *Tnfaip3*$^{+/+}$, *Tnfaip3*$^{I325N/+}$, *Tnfaip3*$^{I325N/I325N}$ male or
1032 female mice. **(B)** Representative H&E and insulin (INS) stained pancreas sections (note
1033 pancreatitis; scale = 100 μm) with **(C)** cumulative insulitis scores (0 = no evidence of
1034 inflammation; 1 = mononuclear cells present, but not infiltrating islet; 2 = 0-25%
1035 mononuclear cell infiltration of islet [peri-insulitis]; 3 = >25% insulitis; 4 = >75% insulitis)
1036 and, **(D)** calculated beta cell mass for *Tnfaip3*$^{+/+}$ and *Tnfaip3*$^{I325N/I325N}$ mice. **(E)** Heat map
1037 depicting mRNA levels for islet early-immediate pro-inflammatory factors[77] measured by
1038 RT-qPCR from islets isolated from individual mice and treated with TNFα for the indicated
1039 times. Values normalised against 0 h *Tnfaip3*$^{+/+}$ islets. Data represents 3 independent islet
1040 preparations with 3-4 biological replicates. **(F)** Islets isolated of the indicated genotypes were
1041 transplanted under the kidney capsule of syngeneic diabetic *Tnfaip3*$^{+/+}$ recipients. When
1042 euglycemia was established comparably by mutant or wild-type islets (see Extended Data
1043 Fig. 12A), a glucose tolerance test was conducted. Following an overnight fast, recipients
1044 received 2 g/kg glucose (i.p.) and blood glucose monitored over time (min). Mean area under
1045 the curve was used for statistical comparison to wild-type. **(G)** At post-operative day 30, islet
1046 grafts were removed and analysed by H&E staining (scale bar = 50 μm) with the fraction of
1047 islet grafts of each genotype exhibiting immune infiltrate shown below. **(H)** Islet grafts
1048 isolated on post-operative day 10 were analysed for indicated mRNAs by RT-qPCR. Gene
1049 expression was calculated using the average wild-type ΔCt value with each data point
1050 representing an individual graft. P values represent Student's *t*-test unless otherwise stated *P
1051 < 0.05; **P < 0.01; ****P < 0.0001.

Extended Data Figures and Tables

Extended Data Fig. 1.

Evolutionary conservation of I207, C243 and I325 positions in A20 protein amongst jawed vertebrates. Aligned amino acid sequence and secondary structure elements of the A20 OTU domain, from [40]. T108, I207, C243 and I325 residues are boxed in red.

1059

Extended Data Fig. 2.

Global distribution of the T108A;I207L *TNFAIP3* haplotype. (A) gnomAD r2.0.2 population allele frequencies for the T108A and I207L missense variants in *TNFAIP3*, with allele counts above each bar (total as denominator). Populations are defined by principal component clustering of samples with individuals of known ancestry: those which do not cluster fall into the OTH group. AFR, African; AMR, Latino; ASJ, Ashkenazi Jew; EAS, East Asian; FIN, Finnish European; NFE, non-Finnish European; OTH, other; SAS, South Asian. The OTH population includes one homozygote, while all other alleles are heterozygous. **(B)** Frequency of the T108A;I207L *TNFAIP3* haplotype within 279 individual genomes from the Simons Genome Diversity Project[22].
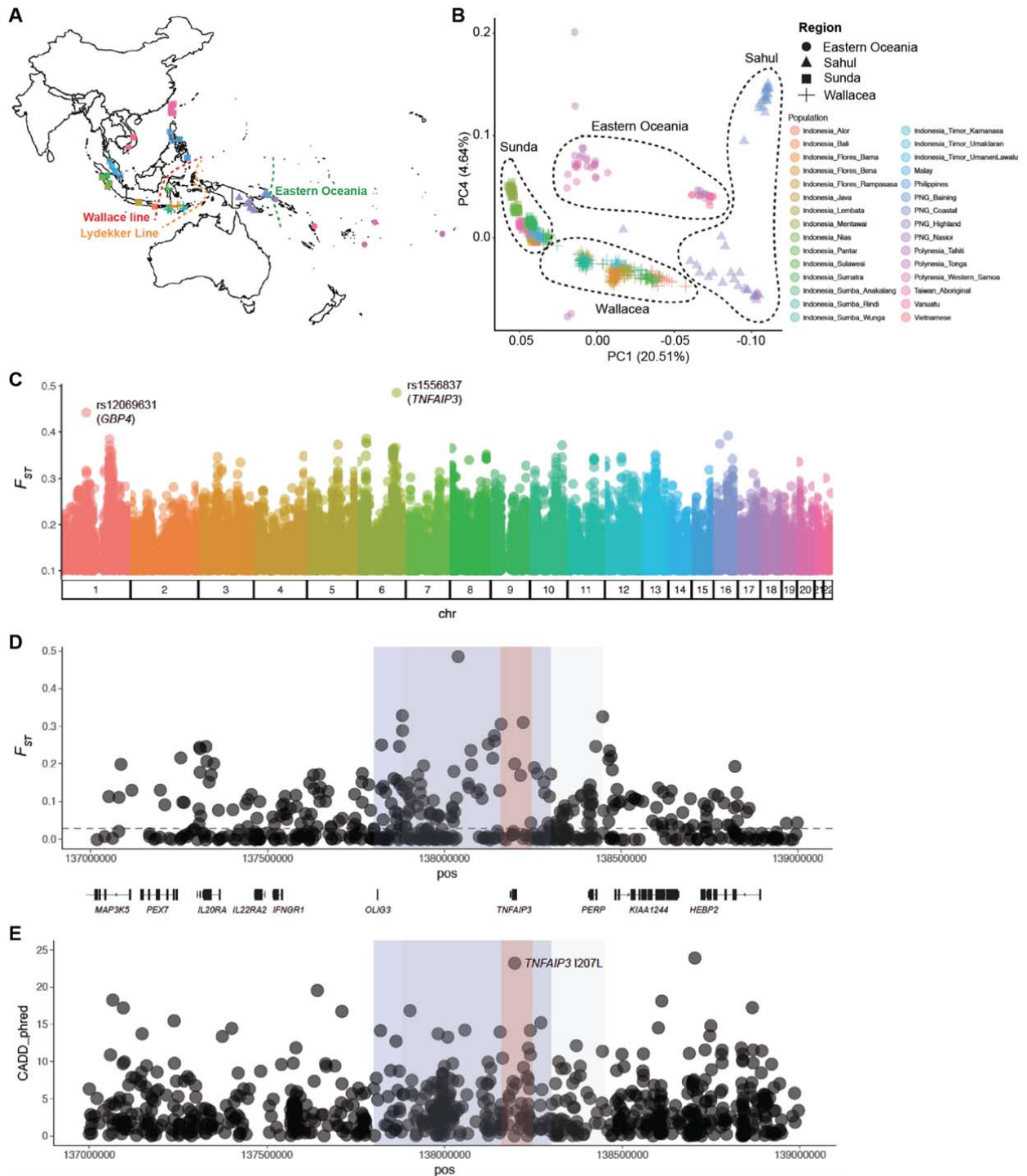
1070

Extended Data Fig. 3.

Population genetics of the Denisovan *TNFAIP3* haplotype. (A) Geographic distribution of samples used for population genetic analyses. Wallace Line (red) [31], Lydekker Line (yellow). Eastern Oceania is defined here as islands east of the Bismarck Archipelago (green line). **(B)** Principal component analysis (PCA), with the proportion of variance explained by each PC indicated on each axis **(C)** Genome-wide F_{ST} values between indigenous populations east and west of the Wallace Line. **(D)** Maximum F_{ST} values on chromosome 6 scores span the

34

1078   *TNFAIP3* locus. Shaded regions correspond to peak F_{ST} values between populations east and
1079   west of the Wallace Line (grey, 6:137881500-138448062), a previously described haplotype
1080   of elevated Denisovan ancestry in Oceanians (blue, 6:137800000-138300000, [25]), and a
1081   putatively adaptively introgressed haplotype in Papuans (red, 6:138160925-138246514, [29]).
1082   **(E)** Phred-scaled CADD scores of all PASS variants with gnomAD allele frequency <0.01
1083   across the extended Denisovan haplotype [27]. Shading as per panel D.
1084
1085
1086
1087
1088
1089
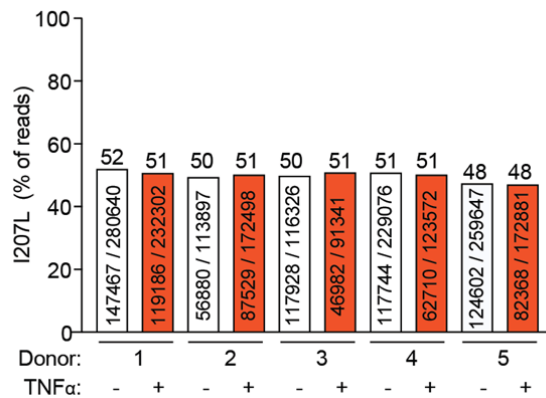
1090

1091   **Extended Data Fig. 4.**

1092   **Relative abundance of Denisovan and modern human *TNFAIP3* mRNA from**
1093   **heterozygous leukocytes.**   Peripheral blood mononuclear cells from five healthy
1094   T108A;I207L heterozygous donors were cultured with (+) or without (-) TNFα for 2 hours,
1095   mRNA isolated and converted to cDNA and amplified with primers in exon 3 and 4 on either
1096   side of the I207 codon. The products were deep sequenced on an Illumina MiSeq. Shown are
1097   the fraction and percentage of reads derived from the T108A;I207L Denisovan allele.
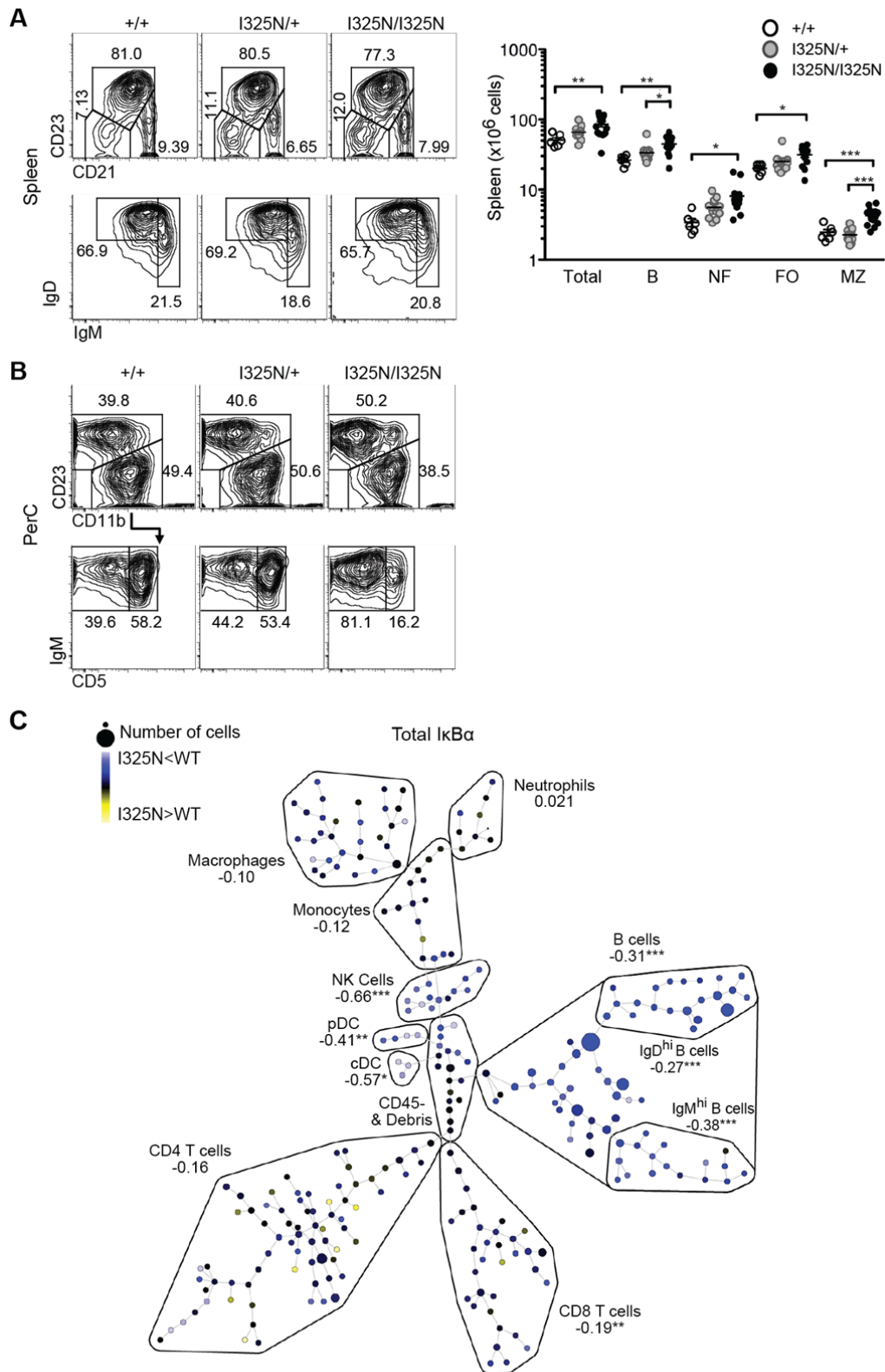
1098

1099   **Extended Data Fig. 5.**

1100 **B cell lymphocytosis induced by the *Tnfaip3^I325N* mutation. (A)** Representative flow
1101 cytometry plots from mice of the indicated genotypes showing total frequency of splenic
1102 CD23$^+$ and CD21$^+$ positive cells (top panel). The bottom panel shows cells subsetted into
1103 IgD$^+$ and IgM$^+$ B cells. Note that the number of splenocyte B cell subsets is increased in
1104 *Tnfaip3^I325N/I325N* mice, shown to the right. **(B)** Representative flow cytometry plots from mice
1105 of the indicated genotypes showing the frequency of CD23$^+$ and CD21$^+$ positive cells in the
1106 peritoneal cavity (top panel). The bottom panel shows frequency of IgM$^+$ and CD45$^+$ B cells.
1107 Number of peritoneal cavity B cell subsets in mice of indicated genotypes is shown in Fig.
1108 2B. **(C)** CYTOF analysis of intracellular IκBα in immune cells. Unstimulated spleen cells
1109 from *Tnfaip3^+/+* or *Tnfaip3^I325N/I325N* mice (*n*=4 per genotype) were individually labeled with
1110 mass-barcodes, mixed, permeabilized and stained with mass-labeled antibodies to a panel of
1111 cell surface markers and intracellular proteins including IκBα, and analyzed by CYTOF mass
1112 spectrometry[59,60]. Spanning-tree Progression Analysis of Density-normalized Events
1113 (SPADE; [61]) analysis was used to resolve leukocyte lineages and subsets, and the relative
1114 intensity of IκBα in each subset was compared between *Tnfaip3^I325N/I325N* and wild-type cell
1115 counterparts. Shown by color and numbers is the mean hyperbolic arcsine (arcsinh) ratio in
1116 minor and major leukocyte subsets. Note that IκBα levels are reduced in B cell subsets
1117 indicating increased NF-κB activation. Significant differences indicated by Student's *t*-test
1118 comparison of major subsets are marked: *$P < 0.05$; **$P < 0.01$; ***$P < 0.001$.
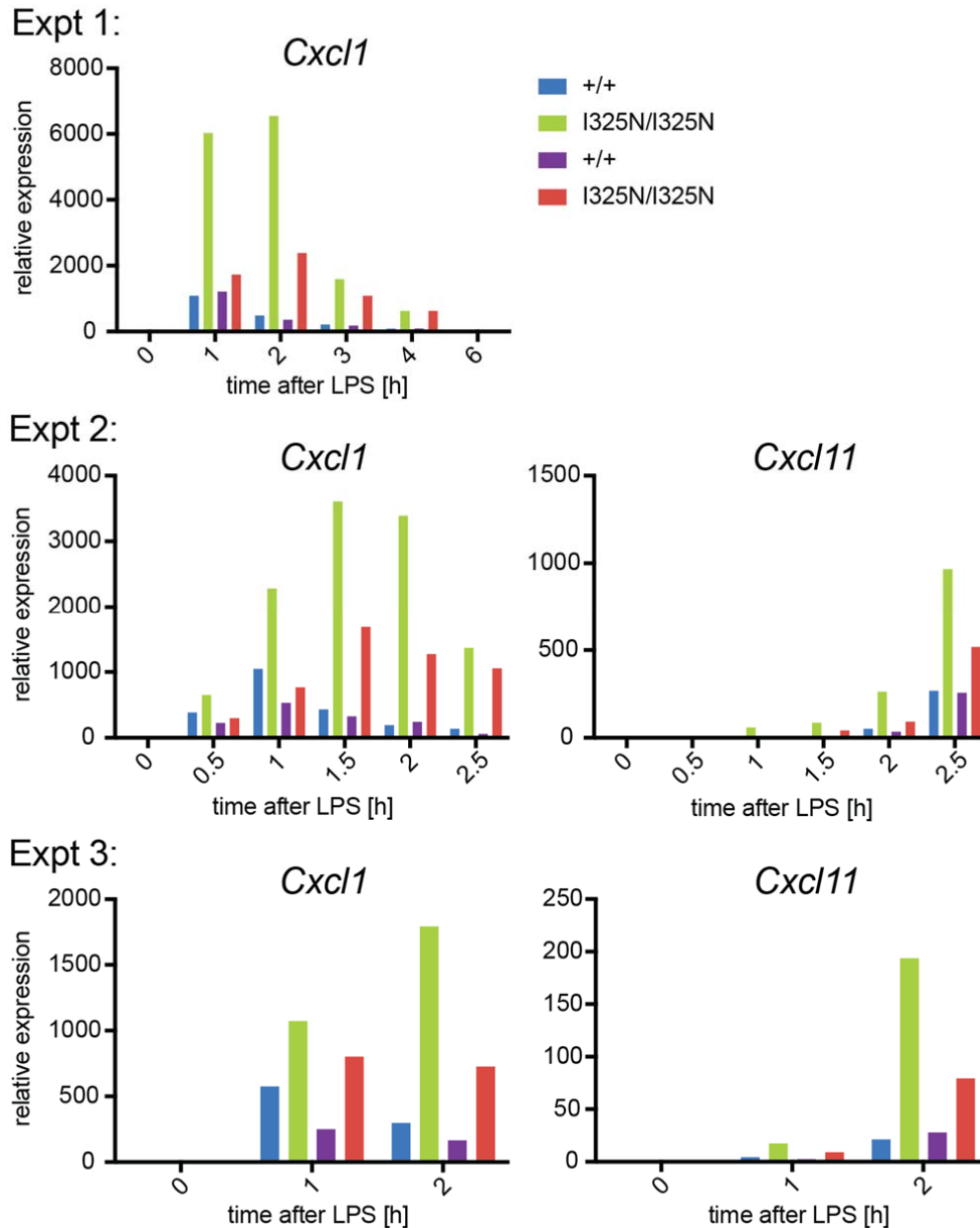
1119

Extended Data Fig. 6.

Exaggerated cytokine production by bone marrow-derived macrophages with the *Tnfaip3*[I325N] mutation. Bone marrow macrophages derived from conditionally *Hoxb8*-immortalized bone marrow progenitor cells were derived from two separate pairs of wild-type and I325N homozygous mice, stimulated with LPS (10ng/ml) for the indicated times, and *Cxcl1* or *Cxcl11* mRNA determined by qPCR relative to *Ef1a* expression. Data are shown from three independent experiments, each with two different mouse donors of each genotype.
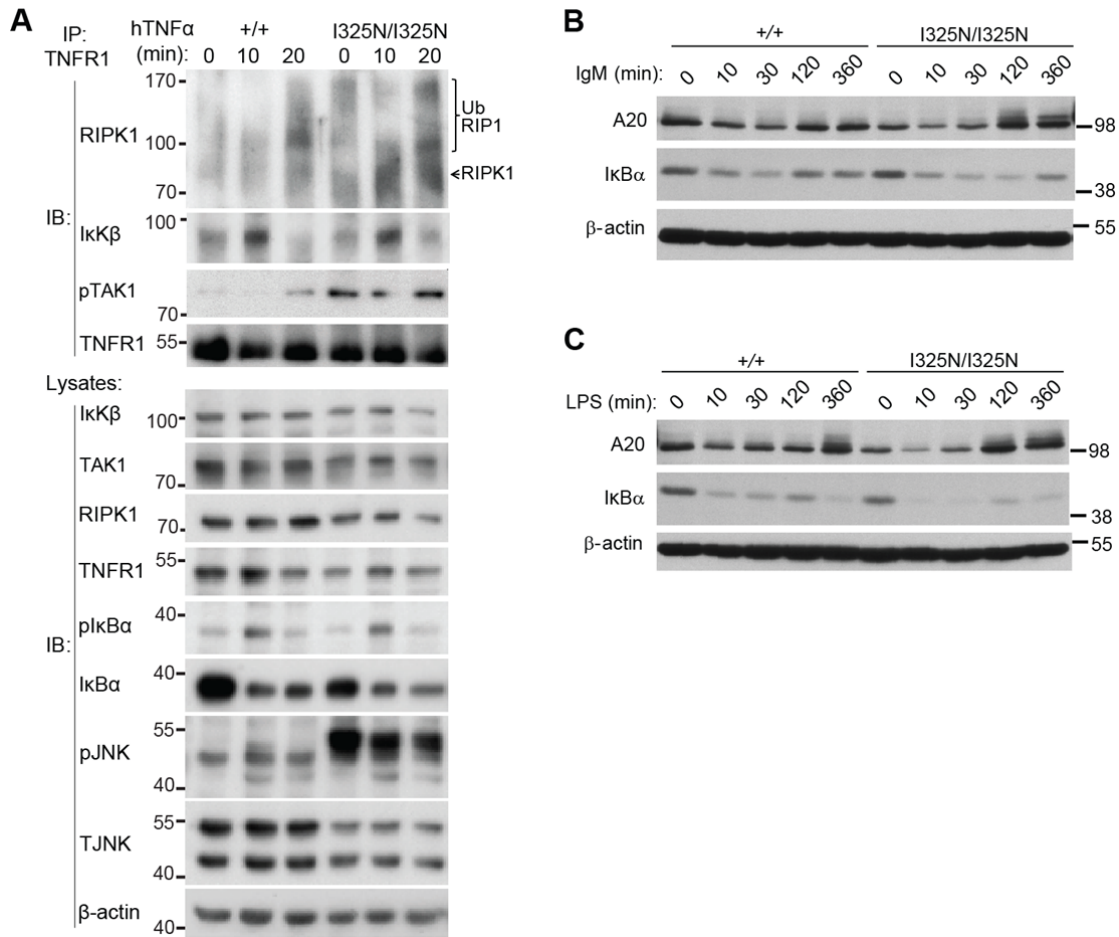
1128

Extended Data Fig. 7.

Prolonged NF-κB signaling in thymocytes and B cells extracted from I325N variant C57BL/6 mice. (A) Representative immunoblot analysis (IB; *n*=3 independent experiments) of canonical NF-κB components following immunoprecipitation (IP) of TNFR1 from lysates of *Tnfaip3*^{+/+} or *Tnfaip3*[I325N/I325N] thymocytes treated with 200 U/ml hTNFα for the indicated times. Following TNFα stimulation RIPK1 was recruited to the TNFR1 complex, with increased high molecular weight polyubiquitinated forms of RIPK1 (UbRIP1) and auto-phosphorylated transforming growth factor β activated kinase-1 [TAK1[78]] in A20[I325N/I325N] thymocytes (A). Mutant thymocytes exhibited a modest increase in IκBα degradation relative to wild-type, and increased JNK phosphorylation (Lysate blots). A similar pattern of enhanced TAK1 activation and JNK phosphorylation was seen in murine embryonic fibroblasts and bone marrow derived macrophages expressing catalytically dead A20 OTU or ZnF4 mutants[18]. **(B, C)** Wild-type (+/+) and I325N homozygous (I325N/I325N) *Tnfaip3* splenic B lymphocytes were stimulated for the indicated times with anti-IgM (B), or lipopolysaccharide (LPS) (C) and lysates analyzed by immunoblotting for A20, IκBα and β-actin (loading control). As observed for mutant thymocytes, B cells exhibited a modest increase in IκBα degradation relative to wild-type.
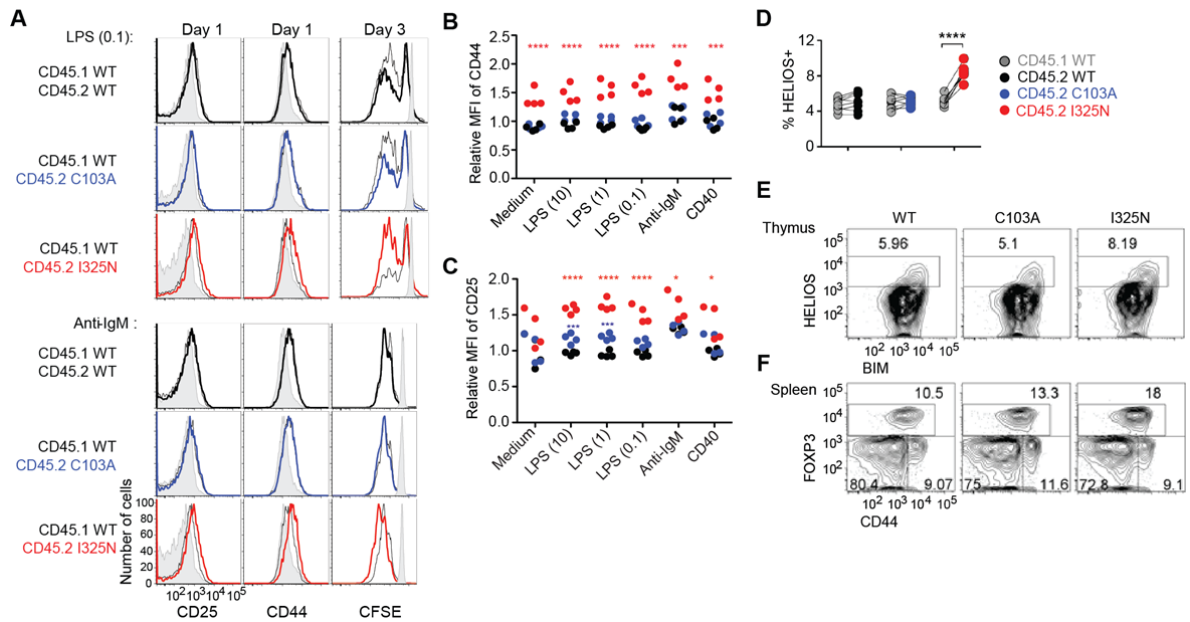
1146

Extended Data Fig. 8.

Cell autonomous exaggeration of B cell activation and Treg formation by Tnfaip3 I325N more than C103A mutations. B6.CD45.1$^+$ wild-type mice were transplanted with a congenic bone marrow mixture from *Tnfaip3*$^{+/+}$ CD45.1$^+$ donors, to provide wild-type lymphocytes as an internal control, and CD45.2$^+$ donors of *Tnfaip3*$^{I325N/I325N}$, *Tnfaip3*$^{C103A/C103A}$ or *Tnfaip3*$^{+/+}$ genotypes. **(A)** Representative flow cytometric histograms of CD25 and CD44 expression on B cells from chimeric mice cultured for 1 day and CFSE dilution after 3 days with 0.1 ug/ml LPS or anti-IgM. Black or colored histograms, CD45.2$^+$ B cells of the indicated *Tnfaip3* genotype; grey line unfilled histograms, CD45.1$^+$ control B cells in the same stimulated culture; grey filled histograms, B cells in a parallel unstimulated culture. **(B, C)** Data from independent mixed chimeric animals showing relative mean fluorescence intensity (MFI) of CD25 or CD44 on CD45.2$^+$ B cells of the indicated genotypes (red, I325N; blue, C103A; black, WT) compared to the co-cultured CD45.1$^+$ wild-type B cells. Statistical analysis by ANOVA: *$P < 0.05$; **$P < 0.01$; ***$P < 0.001$; ****$P < 0.0001$. Figure 2C shows the percentage of CD45.2$^+$ cells of the indicated genotypes among viable B cells, relative to starting percentage, in cultures from individual mixed chimera donors stimulated with 0.1 ug/ml LPS. **(D)** Pairwise comparison of percent HELIOS$^+$ cells among the indicated CD45.2$^+$ and CD45.1$^+$ subsets of CD4$^+$ CD8$^-$ CCR7$^+$ CD24$^+$ FOXP3$^-$ thymocytes from the same chimera. Analysis by paired Student's *t*-test; ****$P < 0.0001$. Compared to the C103A mutation, the I325N mutation exaggerated thymic formation of FOXP3$^+$ CD4$^+$ cells and their Helios$^+$ FOXP3$^-$ precursors, which depend on TCR signaling through CARD11 to NF-κB. **(E, F)** Representative profiles gated on CD45.2$^+$ cells of the indicated *Tnfaip3* genotypes. (E) Analysis of CD4$^+$ CD8$^-$ CCR7$^+$ CD24$^+$ FOXP3$^-$ thymocytes, showing the percentage of immature medullary CD4 T cells induced by strong self-reactivity to express high levels of HELIOS and BIM. (F) Percentage of FOXP3$^+$ CD44$^+$ cells among CD4$^+$ splenic T cells.

40
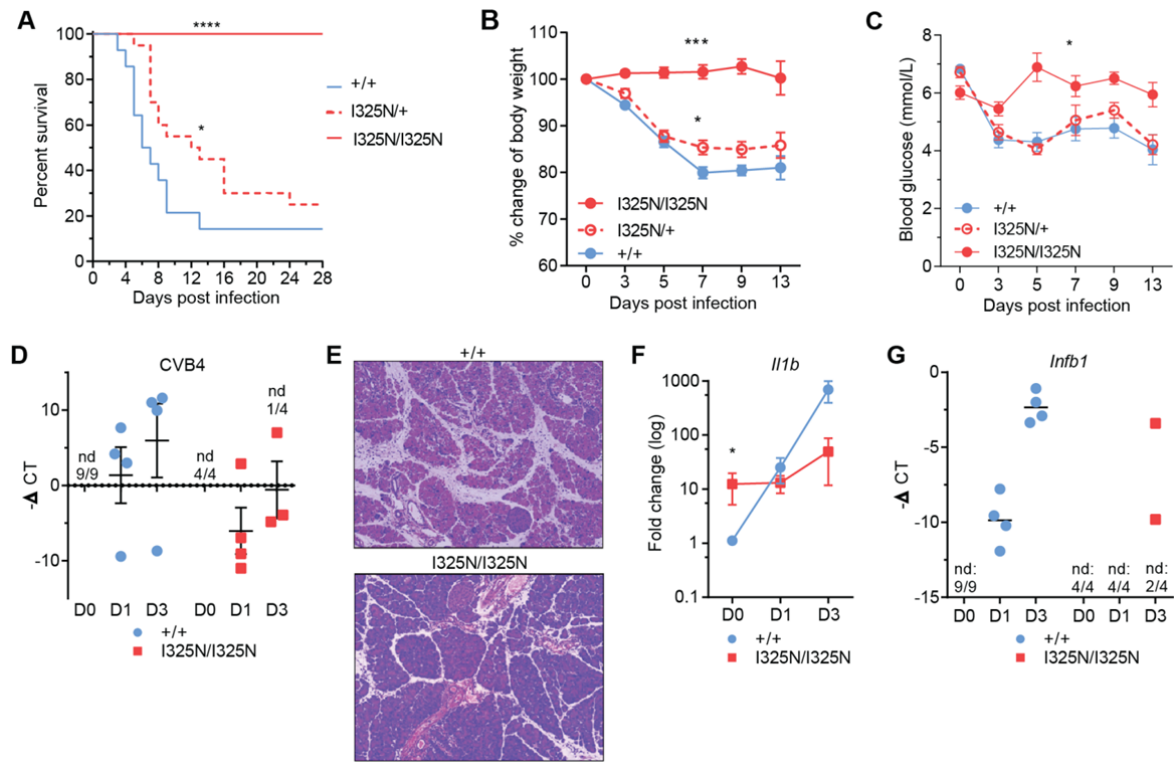
1173

Extended Data Fig. 9.

Increased resistance to Coxsackievirus B4 in A20 I325N mice. Infection of C57BL/6 male mice of the indicated *Tnfaip3* genotypes with 20 plaque forming units (PFU) of Coxsackievirus B4 (CVB4) E2 strain by intraperitoneal injection. **(A)** Kaplan-Meier survival curve showing a mean survival time of 6.5 and 12.5 days for *Tnfaip3*$^{+/+}$ and *Tnfaip3*$^{+/I325N}$ mice, respectively. No *Tnfaip3*$^{I325N/I325N}$ mice succumbed to infection. Significance determined by Log-rank test. **(B)** Percent change in body weight after CVB4 infection and **(C)** Blood glucose levels of mice with indicated *Tnfaip3* genotype, compared to wild-type by area under the curve analysis. **(D)** CVB4 mRNA abundance on indicated days (D0-3) post infection. **(E)** Hematoxylin & eosin stained sections of pancreas from *Tnfaip3*$^{+/+}$ and *Tnfaip3*$^{I325N/I325N}$ mice at post-infection day 9. Note better preserved pancreatic architecture in *Tnfaip3*$^{I325N/I325N}$ mice. Scale bar = 200 μm. **(F, G)** RTPCR analysis for inflammatory genes *Il1b* (F) or *Infb1* (G) at post-infection day 0, 1 and 3. Error bars represent SEM and Student *t*-test used for significance analysis unless otherwise stated, *$P < 0.05$; ***$P < 0.001$.
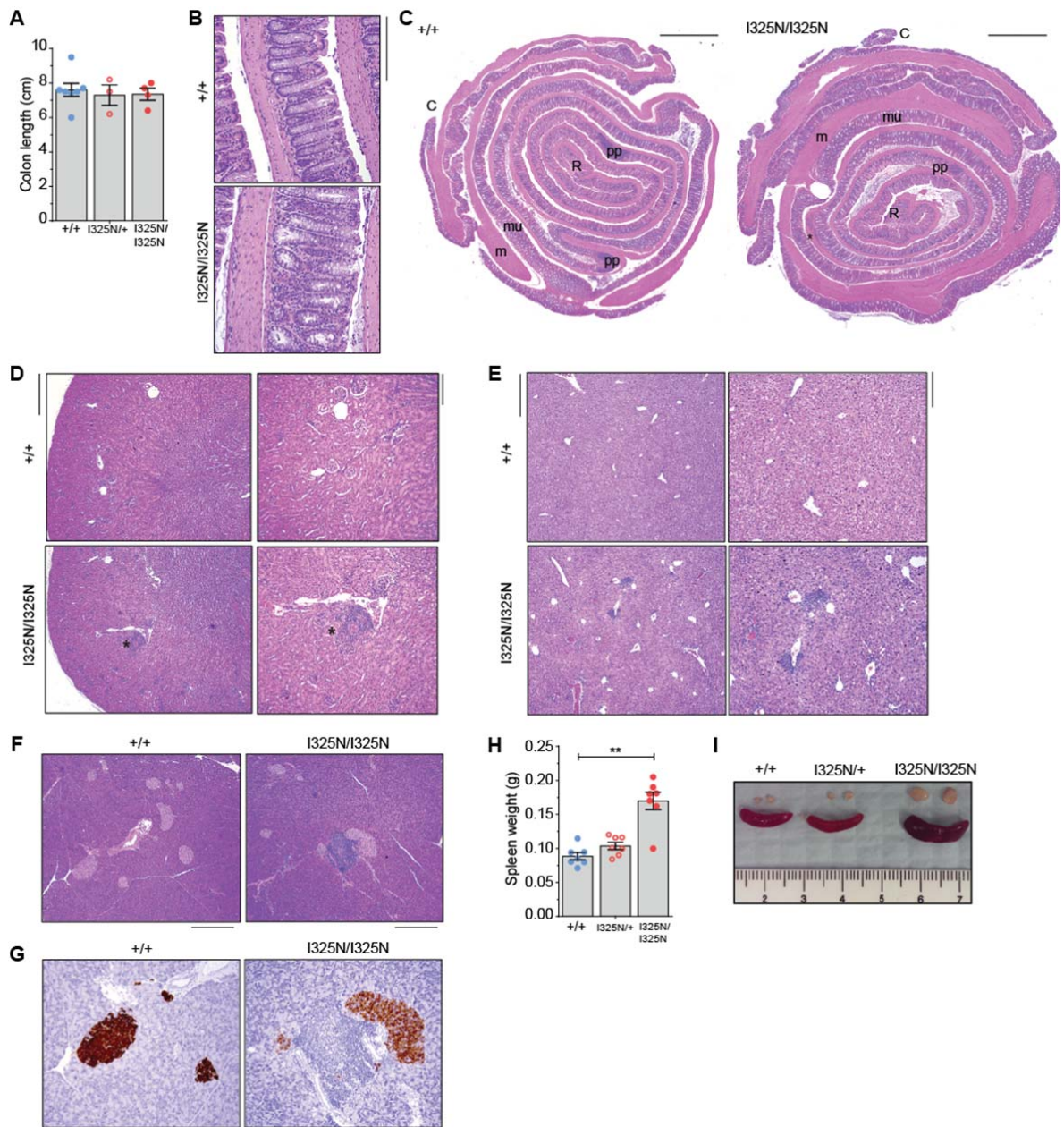
1188

Extended Data Fig. 10.

Histological analysis of tissues from A20^{I325N} mice. (A) Colon length (cm) and **(B)** Hematoxylin and eosin (H&E) stained sections from *Tnfaip3$^{+/+}$* and *Tnfaip3$^{I325N/I325N}$* mice colon (20 X magnification; scale bar = 200 μm) and **(C)** power-mosaic image of whole colon cross section (R=rectum; C=Caecum; m=muscularis; mu=mucosa; pp=Peyer's patches; scale = 1 mm). **(D)** H&E sections of kidney (4 X left images, scale bar = 500 μm; 10 X right images, scale bar = 200 μm) and **(E)** liver (4 X left images, scale bar = 500 μm; 10 X right images, scale bar = 200 μm). **(F)** H&E stained sections of pancreas (10 X images, scale bar = 200 μm) or, **(G)** insulin stained sections (20 X images, scale bar = 100 μm). **(H)** Weight of spleens in grams (g). **(I)** Gross appearance of spleen and salivary glands from *Tnfaip3$^{+/+}$* and *Tnfaip3$^{I325N/I325N}$* mice. Images are representative from n=4 *Tnfaip3$^{+/+}$* and n=4 *Tnfaip3$^{I325N/I325N}$* 16 week old mice. Error bars represent SEM, **$P < 0.01$.
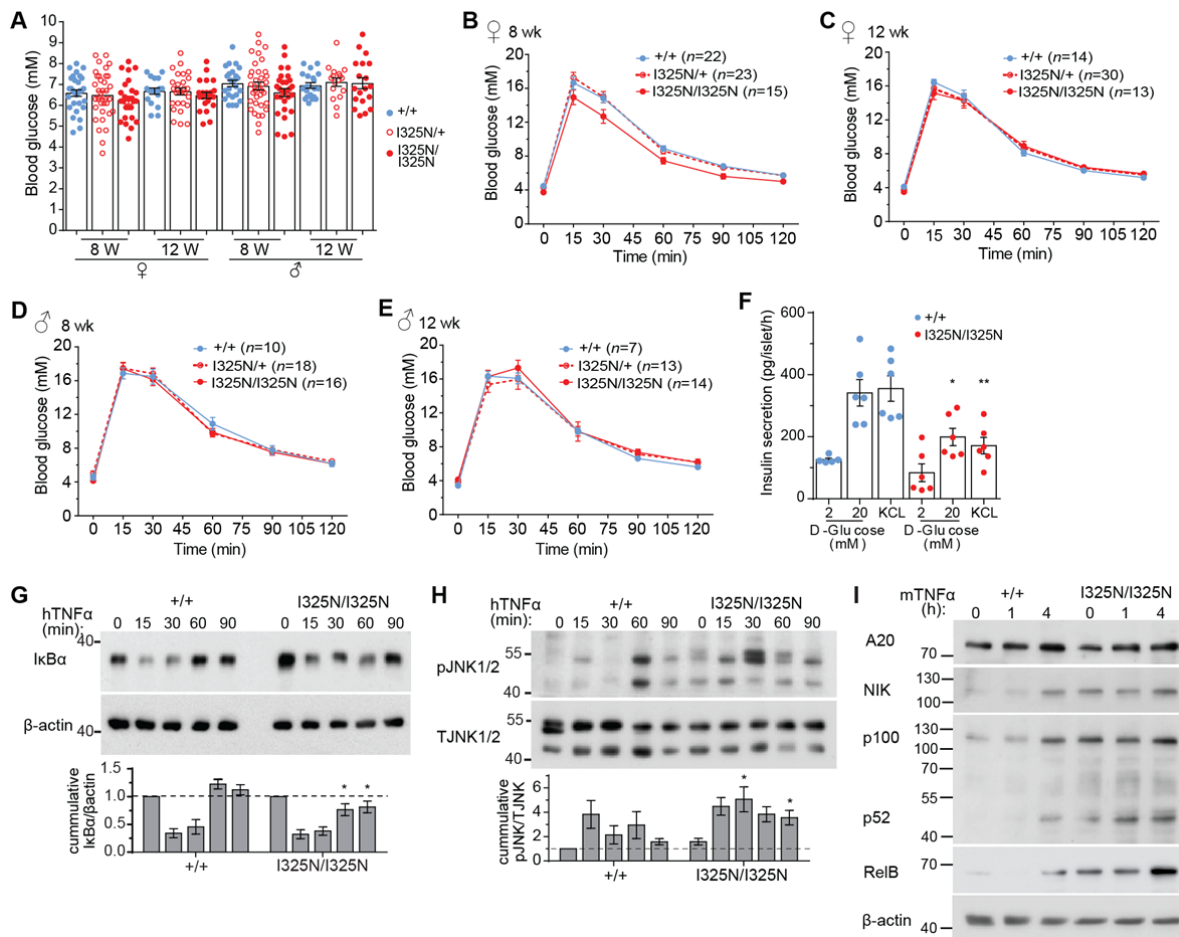
1201

Extended Data Fig. 11.

Glucose homeostasis of A20^{I325N} mice and isolated islets. (A) Random blood glucose levels of *Tnfaip3*$^{+/+}$, *Tnfaip3*$^{I325N/+}$ or *Tnfaip3*$^{I325N/I325N}$ female (♀) or male (♂) mice at 8 or 12 weeks of age. **(B-E)** Blood glucose levels (mM) were monitored following an intraperitoneal injection of glucose (2 g/kg) in 8 (B, D) or 12 week-old (C, E) mice. **(F)** Pancreatic islets were isolated from individual mice of the indicated A20 genotypes and incubated overnight. Following incubation an *in vitro* Glucose-Stimulated Insulin Secretion (GSIS) response in conditions of 2 mM, 20 mM D-glucose, or 25 mM KCl was conducted in separate groups of islets. Error bars represent SEM and Student's *t*-test used for significance between treatments, *$P < 0.05$; **$P < 0.01$. **(G-H)** Pancreatic islets were isolated from individual mice of the indicated A20 genotypes, incubated overnight, and treated with 200 U/ml TNFα for the indicated times. (G) Representative immunoblot for IκBα and β-actin (loading control) or (H) phosphorylated JNK (pJNK) and total JNK (TJNK, loading control). Cumulative densitometry from 5 independent experiments is shown below (n=5 *Tnfaip3*$^{+/+}$ and n=6 *Tnfaip3*$^{I325N/I325N}$ biological replicates). **(I)** Immunoblot for non-canonical NF-κB components NIK, p100/p52 and RelB; representative of 2 independent experiments. *Tnfaip3*$^{I325N/I325N}$ islets exhibited increased activation of the non-canonical NF-κB pathway that can alter beta cell transcriptional programs to favor reduced insulin output [38].
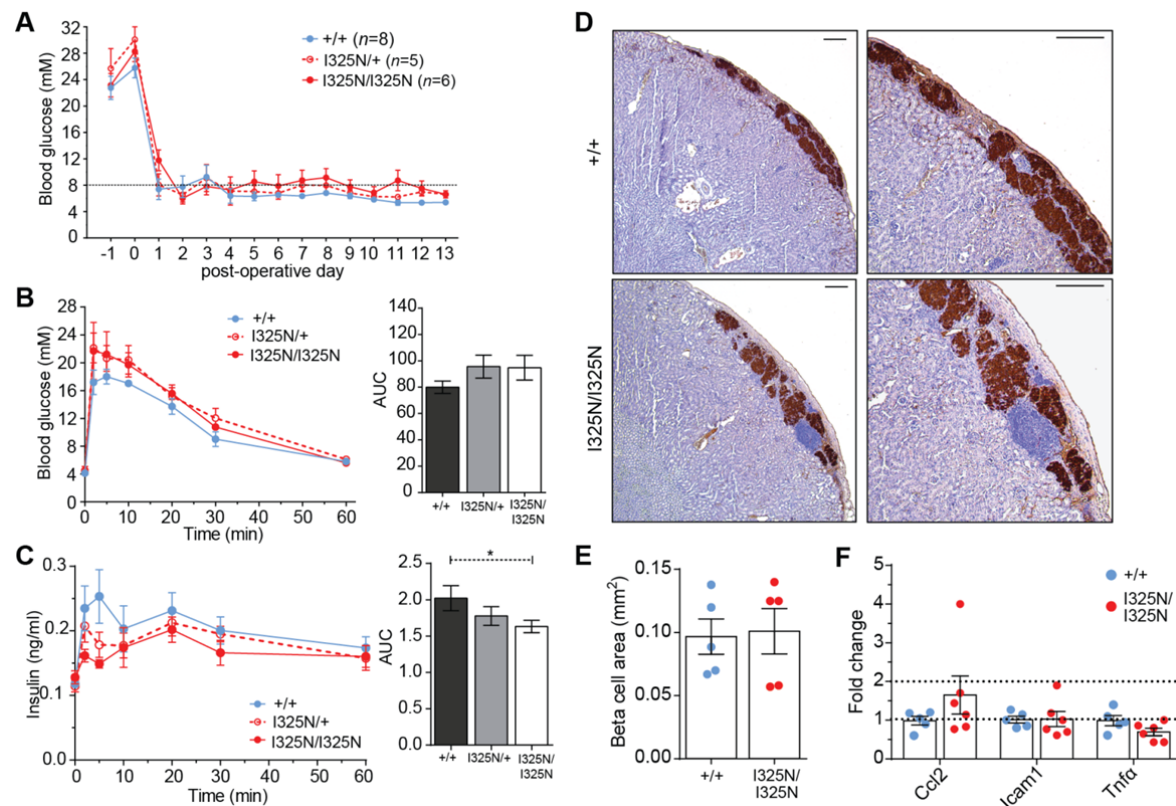
1220

Extended Data Fig. 12.

A20[I325N] islet grafts exhibit a reduced first-phase insulin secretory response compared to wild-type A20 islet grafts independent to beta cell area. (A) Islets isolated from B6 mice of the indicated genotypes were transplanted under the kidney capsule of *Tnfaip3*^{+/+} B6 recipients that had been rendered diabetic with streptozotocin. Mean and SEM blood glucose on the indicated days relative to islet transplantation is shown. **(B-C)** At post-operative day 14 when euglycemia was established, mice were challenged with an (B) intravenous injection of glucose (1 g/kg), and blood glucose monitored over time (min). (C) Blood insulin levels (ng/ml) were also measured at the same time points via an enzyme-linked immunosorbent assay from samples in (B). AUC = area under the curve. Error bars represent SEM and ANOVA used for significance, *$P < 0.05$. **(D)** Insulin immunostaining of wild-type (*Tnfaip3*^{+/+}) or A20 I325N homozygous mutant (*Tnfaip3*[I325N/I325N]) islet grafts transplanted under the kidney capsule of diabetic C57BL/6 mice for 30 days (*Tnfaip3*^{+/+} > *Tnfaip3*^{+/+} n = 5; *Tnfaip3*[I325N/I325N] > *Tnfaip3*^{+/+} n=5). **(E)** Islet graft beta cell area was determined by insulin-positive area quantification in continuous serial graft sections. *Tnfaip3*[I325/I325N] grafts exhibited equivalent insulin-positive graft area, confirming that loss of glucose tolerance (B, C) was due to a defect in insulin secretion. **(F)** *Tnfaip3*^{+/+} or *Tnfaip3*[I325N/I325N] islet grafts from an independent cohort of recipi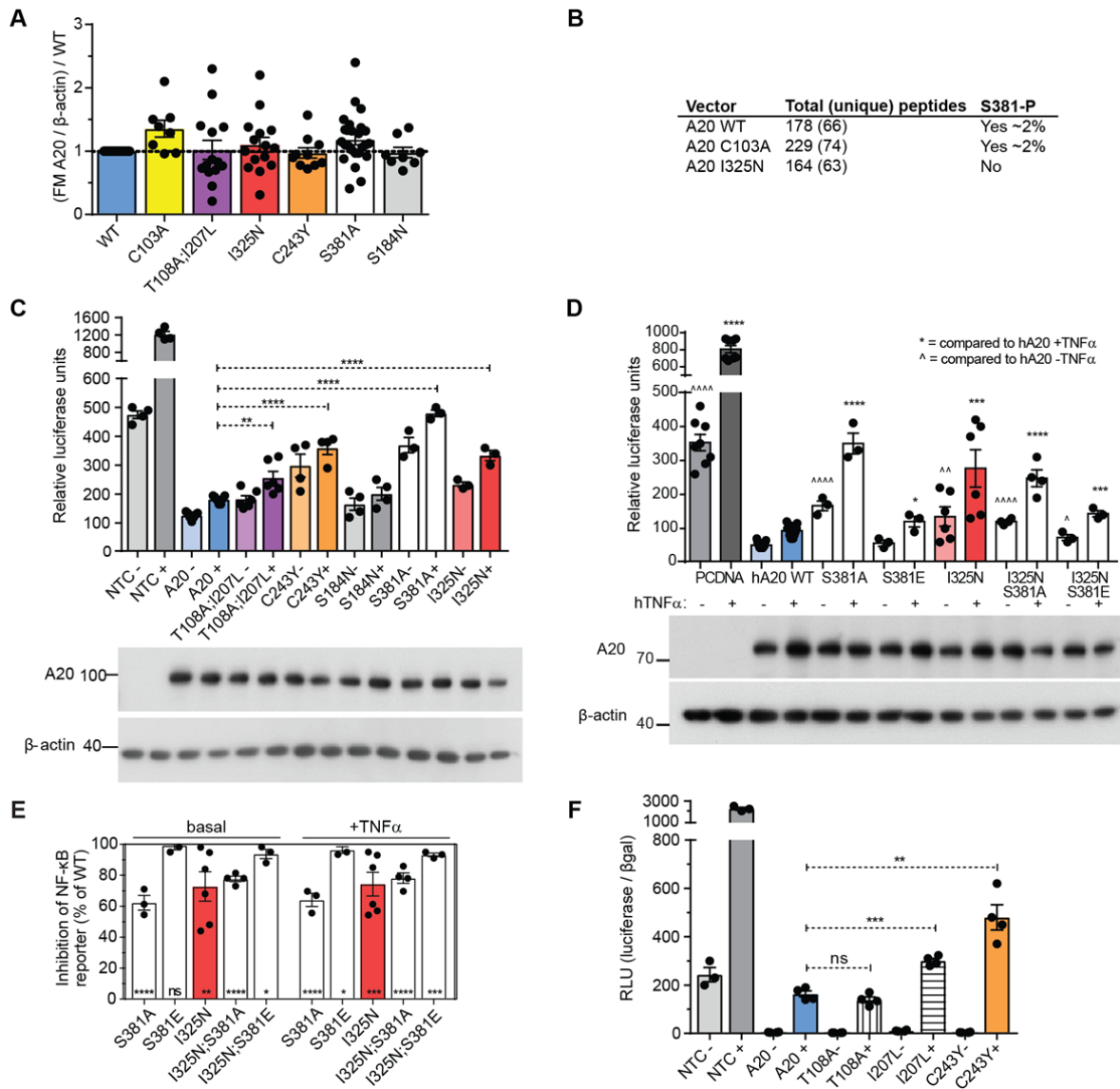ents were isolated on post-operative day 10 and analyzed for the indicated mRNAs by RT-qPCR [77]. The difference in gene expression of indicated islet grafts is shown. Fold change calculated using average wild-type ΔCt value.

| Vector	Total (unique) peptides	S381-P
A20 WT	178 (66)	Yes ~2%
A20 C103A	229 (74)	Yes ~2%
A20 I325N	164 (63)	No

1241

Extended Data Fig. 13.

In vitro analysis of missense variant effects on A20 control of NF-κB. **(A)** A20 accumulation in βTC3 mouse insulinoma cells transfected with wild-type (WT) A20, C103A A20, T108A;I207L A20, I325N A20, C243Y A20, S381A A20 or S184N A20 was determined by densitometry analysis of experimental immunoblots. Fast migratory (A20) 98 kDa A20 was corrected to loading control and compared to WT A20 of the same immunoblot [(FM A20/β-actin)/A20]. **(B)** Results of mass spectrometry analysis of full length WT A20, C103A mutant A20, or I325N mutant A20 expressed in and purified from HEK293 cells and analysed by mass spectrometry for phosphorylation of the indicated residues as per references [18,19]. **(C)** βTC3 cells co-transfected with an NF-κB.luciferase reporter and a CMV.βgal expression construct alone or with PCDNA3.1 encoding human wild-type A20 (hA20 WT; blue), A20 T108A/I207L (purple), A20 C243Y (orange), A20 S184N (grey), A20 I325N (red) or A20 S381A (white). Cells were stimulated with (+) 200 U/ml hTNFα for 8 h or left untreated (-). Data presented as relative luciferase units. Each column represents 3-5 independently transfected aliquots of cells within one experiment marked by circle symbols (representative of 3 independent experiments) and columns are arithmetic means. Statistical

1258   comparison by Student's *t*-test against WT hA20 (blue). **(D-F)** βTC$_3$ cells co-transfected with
1259   a NF-κB.luciferase reporter and a CMV.βgal expression construct alone or with PCDNA3.1
1260   encoding human wild-type A20 (hA20 WT; blue), or (D) A20 I325N variant (I325N; red), or
1261   A20 with serine 381 substituted to non-phosphorylatable alanine (S381A or I325N S381A),
1262   or to phosphomimetic glutamate (S381E or I325N;S381E), (F) or A20 with the point variants
1263   T108A (vertical stripes), I207L (horizontal stripes) or C243Y (orange). Cells were stimulated
1264   with (+) 200 U/ml hTNFα for 8 h or left untreated (-). In (E) the two missense variants in the
1265   Denisovan haplotype, T108A and I207L, are tested individually (cross-hatched columns).
1266   Data presented as relative luciferase units. Each column represents mean of 3-6
1267   independently transfected aliquots of cells within one experiment marked by circle symbols
1268   (representative of 3 independent experiments) and columns are arithmetic means. Statistical
1269   comparison by Student's *t*-test against WT hA20 (blue) with TNFα (+) indicated by * or
1270   without (-) indicated by ^. In (F), data from (D) are presented as inhibition of NF-κB reporter
1271   as a percent of WT A20. Error bars represent SEM, *$P < 0.05$; **$P < 0.01$; ***$P < 0.001$;
1272   ****$P < 0.0001$.
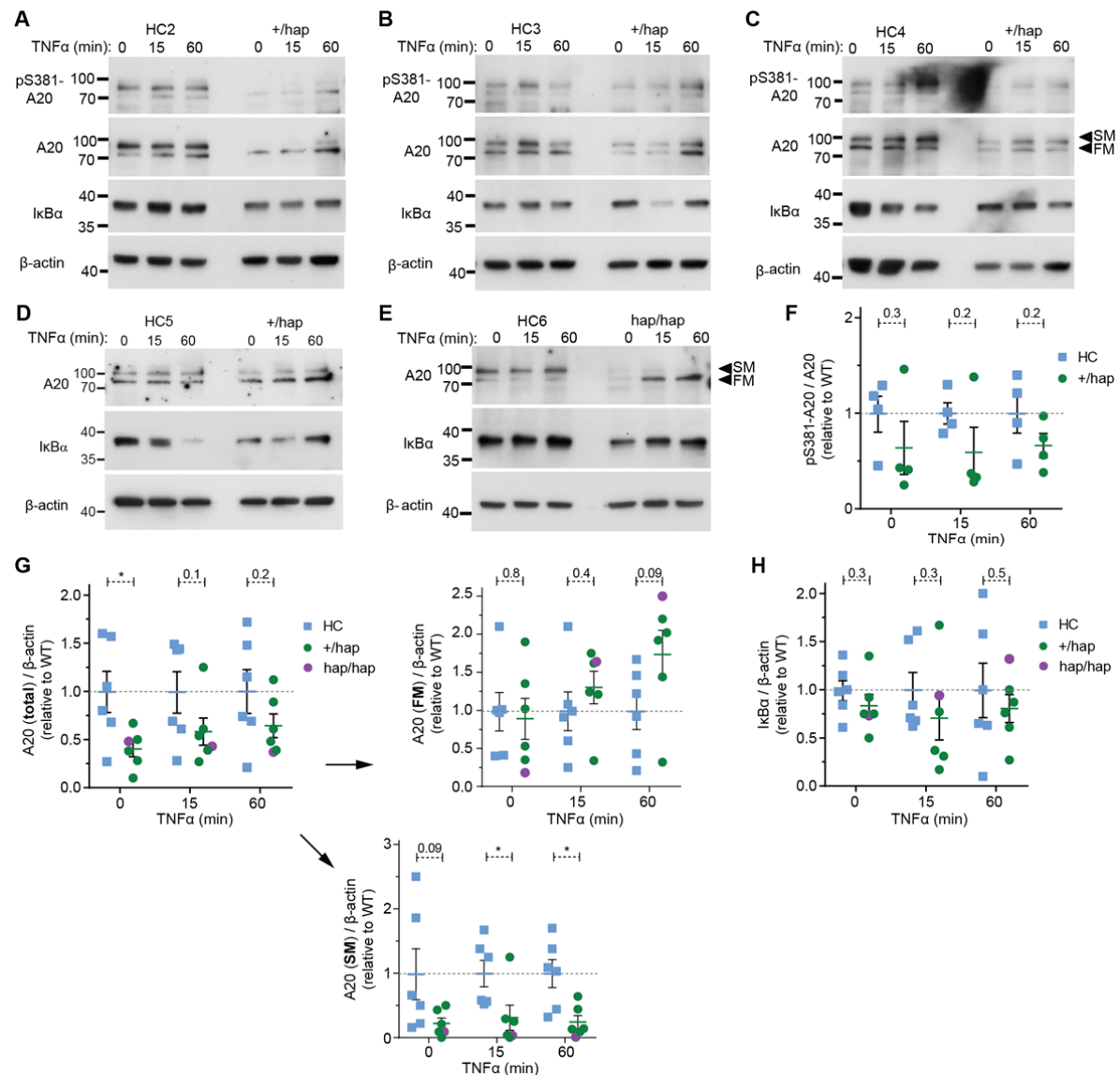
1273

Extended Data Fig. 14.

Immunoblot analysis of peripheral blood mononuclear cells from healthy individuals with the T108A I207L haplotype. (A-E) Immunoblot analysis of peripheral blood mononuclear cells (PBMC) from individuals with the Denisovan *TNFAIP3* haplotype (hap) or without (healthy control donor; HC). PBMCs were left untreated or stimulated with recombinant human TNFα (hTNFα) for 15 or 60 min. Proteins assessed include A20, phosphoserine-A20 (pS381-A20), IκBα and β-actin (loading control). **(F)** Densitometry analysis of pS381-A20 levels in immunoblots A-C and Fig. 4D. Densitometry was calculated by correcting to total A20 present and using the average value from samples without the T108A;I207L haplotype (HC) to compare all samples. **(G)** Densitometry analysis of total A20 levels in immunoblots A-C and Fig. 4D. Densitometry was calculated by correcting to β-actin loading control and using the average WT value to compare all samples. (G) is further divided into fast migrating (FM) or slow migrating (SM) A20. No significant difference is observed for FM A20 between hap or HC individuals. In contrast, a significant difference is observed between hap and HC individuals for SM A20, which correlates with phosphorylated A20 in *in vitro* studies (Fig. 4D, E) [18,19]; consistent with reduced phosphorylation for A20

47

1290   T108A;I2107L. **(H)** Densitometry analysis of IκBα levels in immunoblots A-C and Fig. 4D.
1291   Densitometry was calculated by correcting to β-actin loading control and using the average
1292   value from samples without the T108A;I207L haplotype (HC) to compare all samples. Each
1293   symbol represents an individual lane in immunoblot. Error bars represent SEM and Student's
1294   *t*-test used for significance analysis unless otherwise stated, *$P < 0.05$.
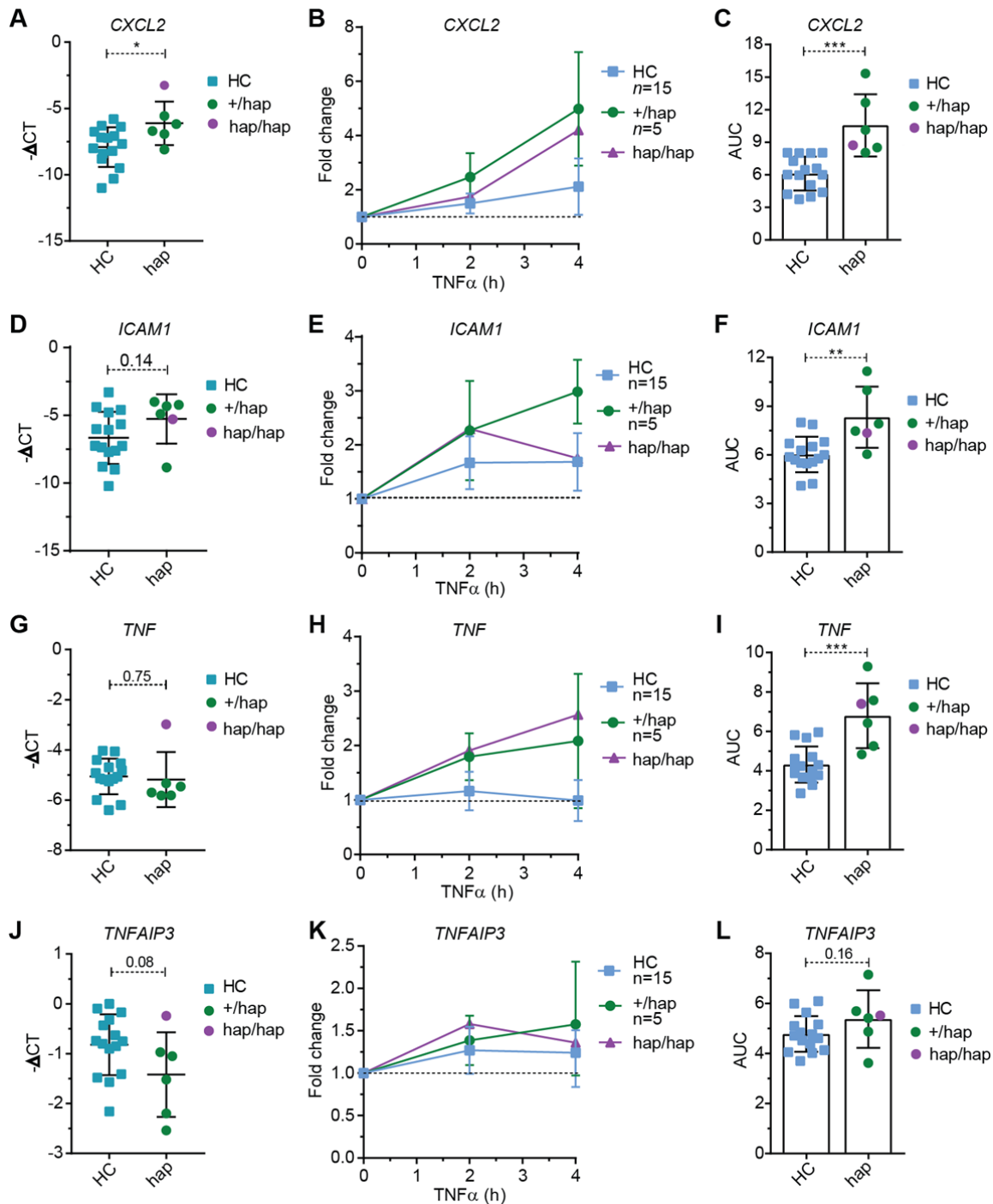
1295

Extended Data Fig. 15.

Peripheral blood mononuclear cells from individuals with the Denisovan *TNFAIP3*
T108A;I207L haplotype are hyper-inflammatory. RT-PCR analysis of *CXCL2*, *ICAM1*,
TNF, and *TNFAIP3* genes expression from peripheral blood mononuclear cells (PBMCs)
from individuals heterozygous (green circles) or homozygous (purple circle) for the
Denisovan *TNFAIP3* haplotype (hap) and 15 healthy control donors (HCs; blue squares),
comparing negative ΔCT basal expression levels **(A, D, G, J)** or induction kinetics following
stimulation with recombinant human TNFα for 0 2 or 4 h **(B, E, H, K).** Fold change was
determined by comparing stimulated values against non-stimulated PBMC preparations

1305   within the same group. Significance between groups was determined by area under the curve

1306   analysis **(C, F, I, L)**. Error bars represent SD and Student's *t*-test used for significance

1307   analysis unless otherwise stated, *P* < 0.05; ***P* < 0.001.
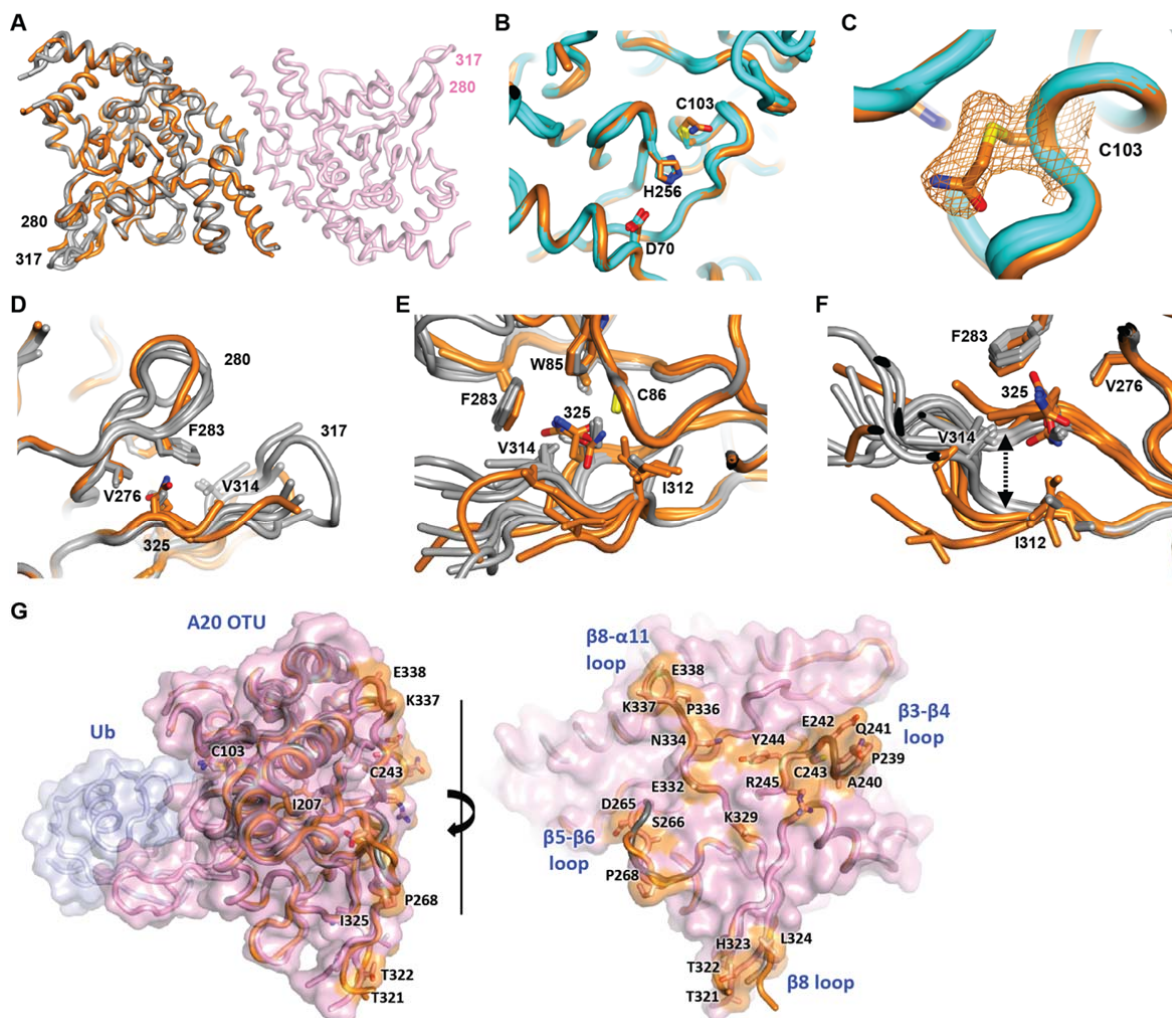
1308

1309 **Extended Data Fig. 16.**

1310 **A20^{I325N} mutation subtly impacts the OTU structure. (A)** Structures of human I325N
1311 variant (orange) and wild-type (WT; grey) A20 OTU domains superposed (each with 6
1312 molecules per asymmetric unit). The dimer partner of one of these is shown in pink. Loop
1313 317 and 280 are indicated on the periphery. **(B)** The I325N substitution does not alter the fold
1314 of the putative catalytic triad (orange cartoon and sticks) compared to previously published
1315 wild-type structures (cyan cartoon and sticks; PDB entries 3DKB, 2VFJ and 3ZJD). **(C)** The
1316 fold is additionally unperturbed by acetamidylation of C103 (orange mesh; 2mFo-DFc
1317 composite omit map contoured at 1.2 sigma). **(D-F)** The I325N substituted side-chain sits at
1318 the base of the β7-β8 loop containing residue 317, in a pocket also lined by the β6-α9 loop
1319 containing residue 280 (D). Adjacent hydrophobic residues include W85, V276, F283, I312,
1320 V314 (E). The I325N substitution results in the base of the β7-β8 loop splaying apart (F,
1321 arrow), increasing β7-β8 loop disorder. **(G)** Structures of human I325N variant (orange) and
1322 wild-type (WT; grey) A20 OTU domains superposed on the wild-type OTU-ubiquitin
1323 structure 5LRX [42]. Conserved residues on the posterior surface are coloured orange. The β3-
1324 β4 loop containing the C243Y mutation and the structured base of the β7-β8 loop containing
1325 the I325N mutation are marked.

51
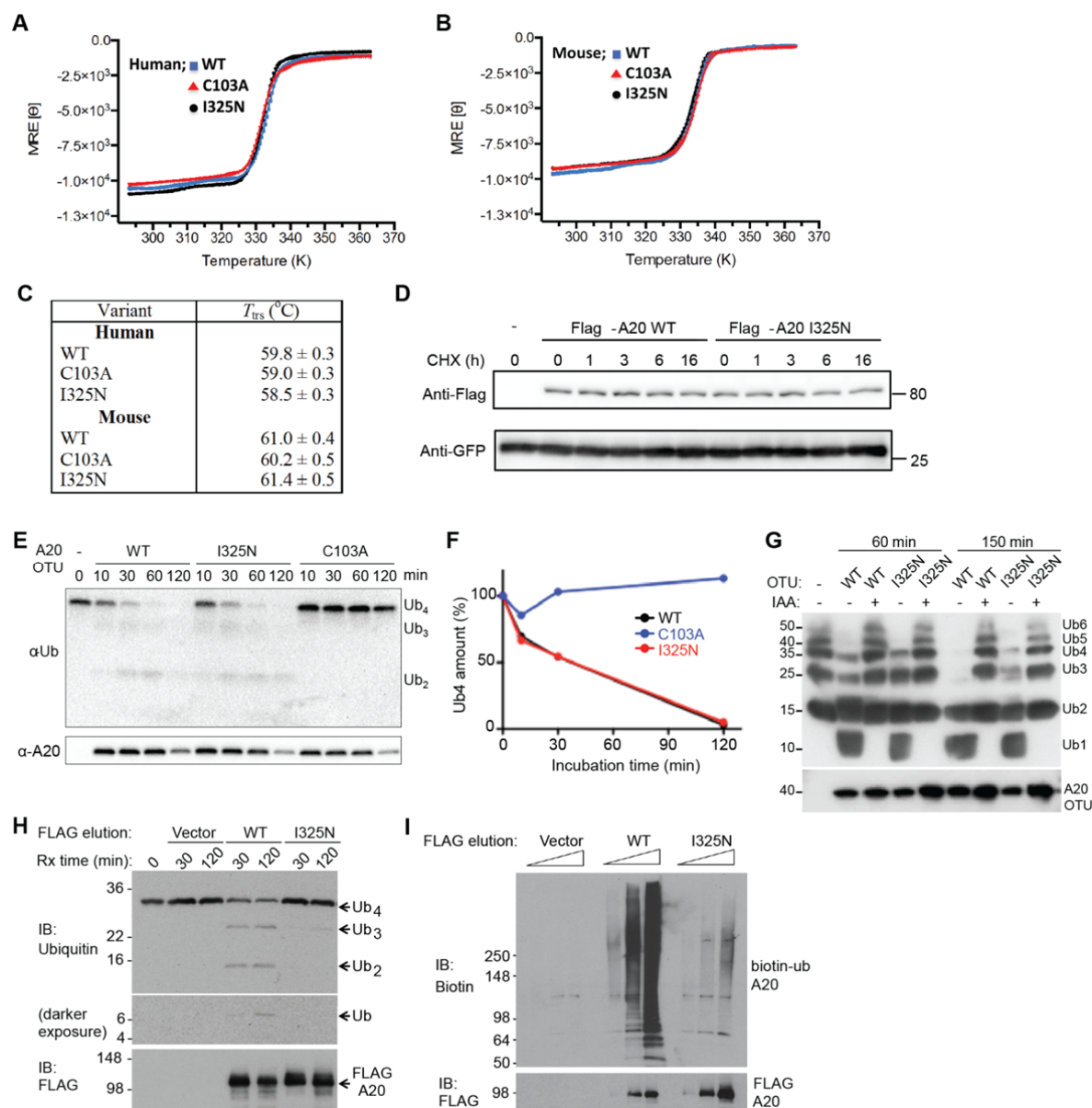
1326

Extended Data Fig. 17.

Molecular characterization of A20 I325N and A20 C103A. (A-B) Thermal stability of mouse and human WT, C103A, and I325N variants were examined using circular dichroism, where mean residue ellipticity (MRE) was measured at 220 nm as a function of temperature as solutions were heated at a rate of 1° C/min. Human (A) or mouse (B) A20 OTU residues 1-370; WT (blue squares), C103A (red triangles), I325N (black circles). Curves were fit by linear regression. **(C)** Unfolding transitions temperature (T_{trs}) of human A20 OTU variants (residues 1-370) and mouse variants (residues 1-360), derived from the fit of the curves in (A) and (B). **(D)** HEK293T cells were transfected with bicistronic retrovirus vector pMXs-IRES-GFP, expressing FLAG-tagged mouse full-length TNFAIP3 wild-type or I325N. Each group of transfected cells was replated 24 h after transfection and incubated with 10 μM of cycloheximide (CHX) for the indicated times before harvesting. Lysates were probed with anti-FLAG and anti-GFP antibodies. **(E, F)** Reactions containing K48-linked tetra-ubiquitin (Ub$_4$) and *E. coli*-expressed and purified WT or I325N A20 OTU domain, or the catalytically

1341 deactivated A20 OTU domain, C103A, were incubated for the indicated times.

1342 Depolymerization of polyubiquitin was detected by immunoblotting for ubiquitin and A20;

1343 representative of two independent experiments. **(G)** Reactions containing mixed Ub_2-Ub_6

1344 K48-linked polyubiquitin chains and *E. coli*-expressed and purified WT or I325N A20 OTU

1345 domain ± iodoacetamide (IA) treatment were incubated at 37°C for 60 or 150 minutes.

1346 Depolymerization of polyubiquitin was detected by immunoblotting for ubiquitin and the N-

1347 terminus of A20; representative of 4 independent experiments. **(H, I)** Flag-tagged full length

1348 human A20 proteins (WT or I325N mutant) were expressed in HEK-293T cells and purified

1349 as previously described [14]. Purified A20 proteins were tested for K63-linked tetra-ubiquitin

1350 depolymerization (H) and *in vitro* ubiquitination assay (I).
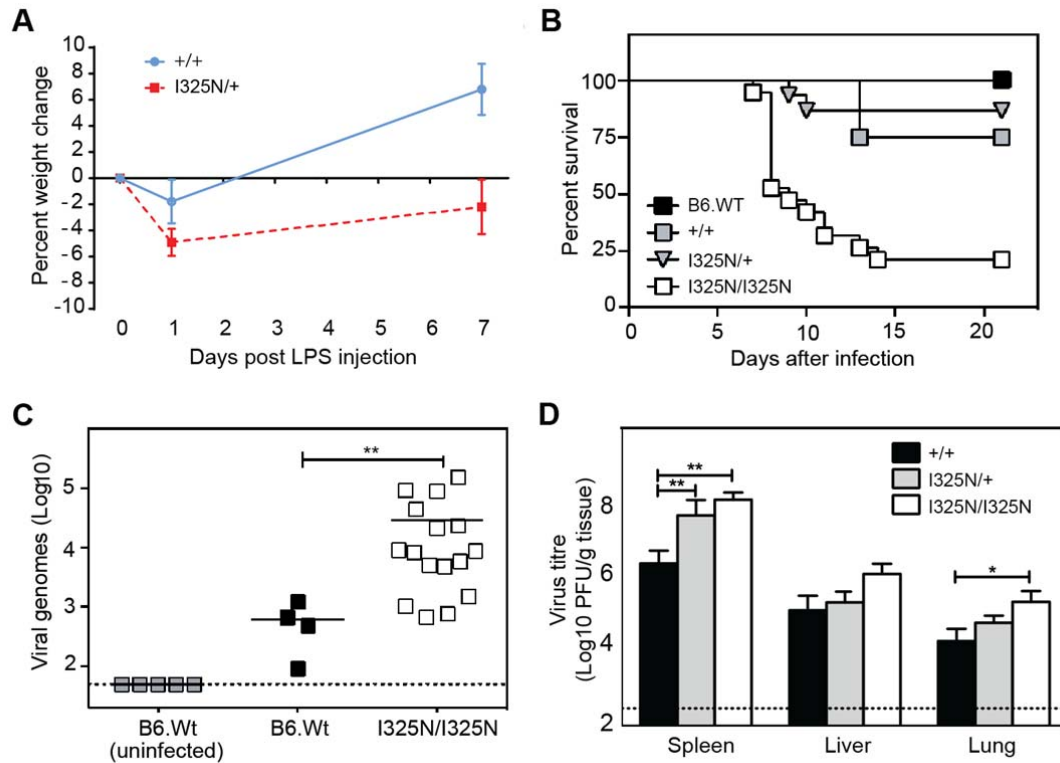
1351

Extended Data Fig. 18.

A20 I325N are susceptible to LPS injection and poxvirus infection. (A) Daily body weights for *Tnfaip3*$^{+/+}$ or *Tnfaip3*$^{I325N/+}$ mice administered 50 µg bacterial LPS by intraperitoneal injection. (B-D) Ectromelia virus infection of B6 male siblings of the indicated *Tnfaip3* genotypes and wild-type B6 control mice, showing **(B)** Kaplan-Meyer survival plots and **(C)** viral load in blood on day 8; **$P < 0.005$ by unpaired *t* test. **(D)** Virus load in spleen, liver and lung, respectively. Data expressed as mean ± SEM; data was log-transformed and statistical significance determined by 2-way ANOVA; *$P < 0.05$, **$P < 0.01$. Dotted lines in (C, D) denote limit of detection.
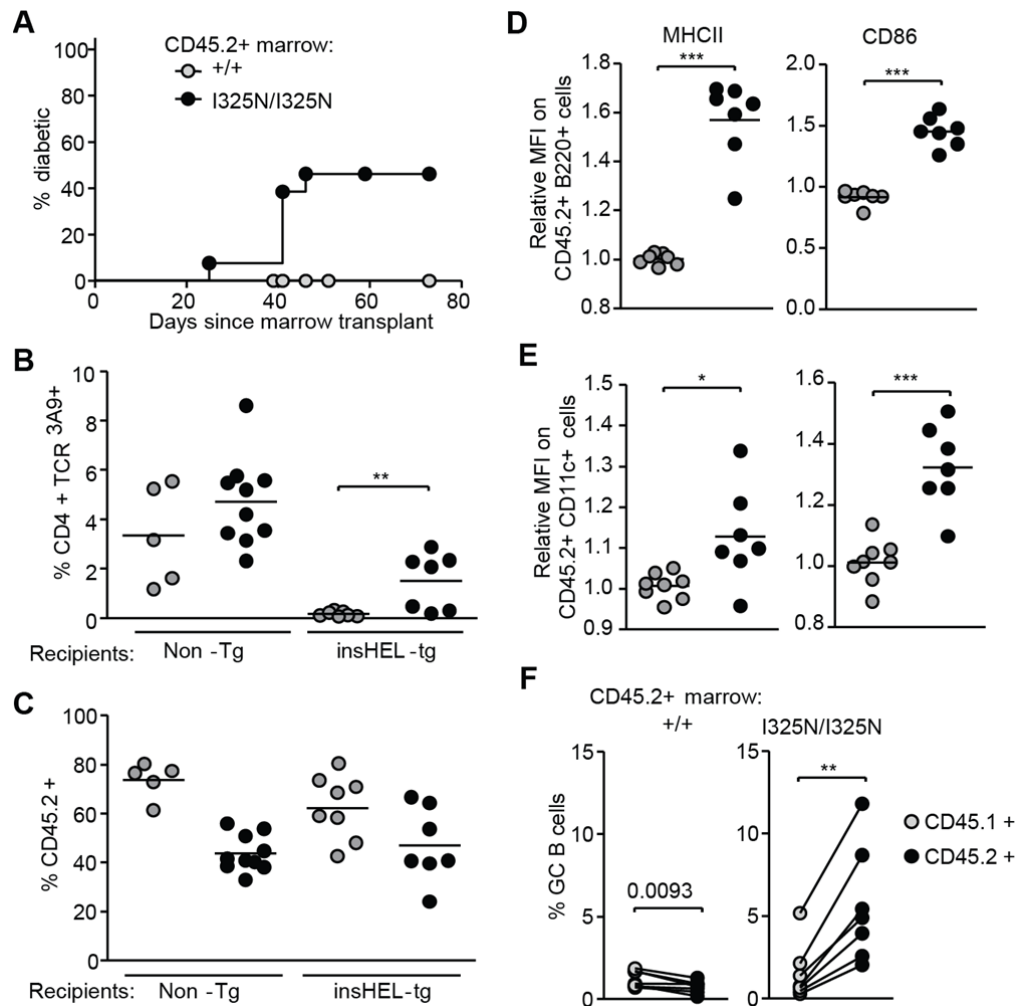
1361

Extended Data Fig. 19.

Diminished tolerance to self-antigen caused by mutant A20. InsHEL-transgenic mice or non-transgenic controls, both with wild-type A20 in pancreatic islets, were transplanted with a congenic bone marrow mixture from $Tnfaip3^{+/+}$ CD45.1$^+$ TCR^{3A9}-transgenic donors, to serve as an internal control, and CD45.2 TCR^{3A9}-transgenic donors with either $Tnfaip3^{I325N/I325N}$ (black circles) or $Tnfaip3^{+/+}$ (grey circles) genotype. **(A)** Incidence of diabetes in insHEL-transgenic recipients as a function of time after transplantation (n=12 chimeras for +/+ and 14 chimeras for I325N/I325N pooled from 2 separate experiments). **(B)** Frequency of TCR^{3A9} positive CD4$^+$ T cells among CD45.2$^+$ $Tnfaip3^{+/+}$ (grey circles) or $Tnfaip3^{I325N/I325N}$ (black circles) lymphocytes in pancreatic lymph nodes. Test recipients expressed the insHEL antigen in pancreatic islets (insHEL-transgenic), while parallel non-transgenic recipients lacked the autoantigen. **(C)** Percentage of CD45.2$^+$ $Tnfaip3^{+/+}$ (grey circles) or $Tnfaip3^{I325N/I325N}$ (black circles) cells among TCR^{3A9+} CD4$^+$ T cells in spleen. **(D-F)** Analysis of insHEL transgenic recipients. Relative mean fluorescence intensity (MFI) of staining for cell surface MHC class II or CD86 on CD45.2$^+$ $Tnfaip3^{+/+}$ (grey circles) or $Tnfaip3^{I325N/I325N}$ (black circles) B cells (D) or CD11c$^+$ dendritic cells (E), compared to CD45.1$^+$ $Tnfaip3^{+/+}$ B cells or dendritic cells in the same sample. **(F)** Frequency of germinal center (GC) B cells among CD45.2+ B cells (black circles) compared to the frequency among CD45.1$^+$ $Tnfaip3^{+/+}$ B cells in the same animal (linked by lines). Left panel, CD45.2 $Tnfaip3^{+/+}$ marrow donor; right panel, CD45.2 $Tnfaip3^{I325N/I325N}$ marrow donor. In (B-F),

1382   each symbol, or pair of symbols joined by a line, represents one chimeric mouse, all analyzed

1383   in a single experiment. Statistical analysis by 2-tailed Student's *t*-tests: $*P < 0.05$; $**P <$

1384 0.01; $***P < 0.001$.

1385
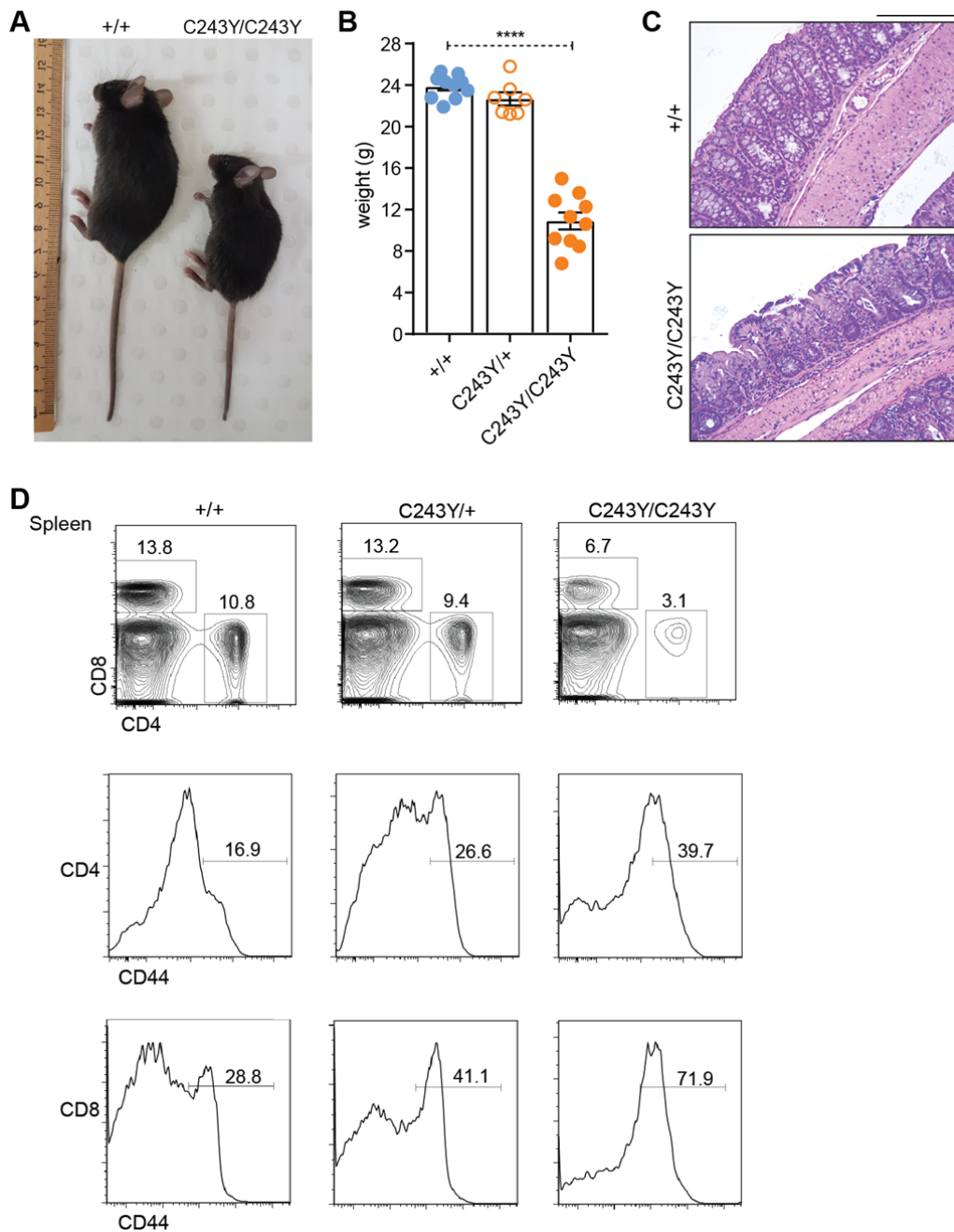
1386

Extended Data Fig. 20.

Histological analysis and immune phenotyping of A20^{C243Y} mice. (A) Representative photo of 8 week-old female *Tnfaip3*$^{+/+}$ and *Tnfaip3*$^{C243Y/C243Y}$ mice. Statistical analysis by one-way ANOVA: ****$P < 0.0001$. **(B)** Weights (g) 8 week-old male *Tnfaip3*$^{+/+}$, *Tnfaip3*$^{C243Y/C243Y}$ and *Tnfaip3*$^{C243Y/C243Y}$ mice. **(C)** Hematoxylin and eosin stained sections of colon from representative female mice in (A) (scale = 200 μm). **(D)** Flow cytometry of the percent CD4$^+$ and CD8$^+$ splenocytes (top panel) and the percentage of each subset that are CD44^{hi} activated/memory cells (histograms).

1395

1396   **Extended Data Table 1.**

1397   Allele frequencies of the Denisovan T108A;I207L haplotype in the Simons Genome
1398   Diversity Project[22], as presented in (Extended Data Fig. 2B).

Region	Denisovan *TNFAIP3* alleles	Total *TNFAIP3* alleles	Denisovan allele frequency
Africa	0	88	0.00
West Eurasia	0	150	0.00
Central Asia	0	54	0.00
South Asia	0	78	0.00
East Asia	0	94	0.00
Americas	0	44	0.00
Oceania & Island SE Asia:	23	50	0.46
(Brunei)	1	4	0.25
(Australia)	1	4	0.25
(Papua New Guinea)	19	30	0.63
(Bougainville)	1	4	0.25
(New Zealand)	1	2	0.50

1399

1400 **Extended Data Table 2.**

1401 Polymorphic observed (black) and imputed (red) variants within a putatively adaptively
1402 introgressed haplotype in Melanesians (6:138160925-138246514, [29]). Ancestral, modern
1403 human (b37), Denisovan, and Altai Neanderthal genotypes are shown at each position for
1404 comparison. Genomic coordinates are based upon the hg19 reference.

Chr	Position	rsID	Missense	Ancestral	b37	Denisovan	Altai Neanderthal
6	138161013	rs6918329		G	A	G	G
6	138174328	rs2027276		C	A	A	C
6	138190154	rs3757173		G	A	A	G
6	138195402	rs596493		C	T	C	C
6	138196008	rs376205580	T108A	A	A	G	A
6	138196957	rs141807543	I207L	A	A	C	A
6	138223082	rs17066926		C	T	C	C
6	138241185	rs4895499		G	A	G	G

1405

1406 **Extended Data Table 3.**

1407 Mouse primers used for qRT-PCR analysis of genes. Designed using Primer3 with sequences
1408 obtained from GenBank and synthesised by Sigma Aldrich (Australia). Primers from Roche
1409 Universal ProbeLibrary (UPL) System Assay are indicated.

Gene	Primer sequence
Tnfaip3	F-5'-CCTGTCACCAACGCTCCAAG-3' R-5'-ATTTCCAGTCCGGTGGCAAG-3'
Ccl2	F- 5'-GGTCCCTGTCATGCTTCTGG-3' R- 5'-CCTGCTGCTGGTGATCCTCT-3'
Cph2	F- 5'-TGGACCAAACACAAACGGTTCC-3' R- 5'-ACATTGCGAGCAGATGGGGT-3'
Cxcl1	F- 5'-TGGCTGGGATTCACCTCAAG-3' R- 5'-TATGACTTCGGTTTGGGTGCAG-3'
Cxcl10	F- 5'-GACGGGCCAGTGAGAATGAG-3' R- 5'-GTGTGTGCGTGGCTTCACTC-3'
Icam1	F- 5'-CCATGGGAATGTCACCAGGA-3' R- 5'-ATCACGAGGCCCACAATGAC-3'
Il6	F- 5'-TCCTTCCTACCCCAATTTCCAA-3' R- 5'-TGGATGGTCTTGGTCCTTAGCC-3'
Il1b UPL probe #38	F- 5'-AGTTGACGGACCCCAAAAG-3' R- 5'-AGCTGGATGCTCTCATCAGG-3'
Rpl19 UPL probe #46	F- 5'-CCACAAGCTCTTTCCTTTCG-3' R- 5'-GGATCCAACCAGACCTTCTTT-3'
Il6 UPL probe #28	F- 5'-GCTACCAAACTGGATATAATCAGGA-3' R- 5'-CCAGGTAGCTATGGTACTCCAGAA-3'
CVB4 UPL probe #41	F- 5'-CCCGGACCGAGTATCAATAA-3' R- 5'-CCGGGTAACGAACGGTTT-3'
Ifnb UPL probe #78	F- 5'-CACAGCCCTCTCCATCAACTA-3' R- 5'-CATTTCCGAATGTTCGTCCT-3'

1410

1411 **Extended Data Table 4.**

1412 Human primers used for qRT-PCR analysis of genes. Designed using Primer3with sequences
1413 obtained from GenBank and synthesised by Sigma Aldrich (Australia).

TNFAIP3	F- 5'-AACGAACGGTGACGGCAAT-3' R- 5'-GAAGTCCACTTCGGGCCAT-3'
TNF	F- 5'-TCCCCTGGAAAGGACACCAT-3' R- 5'GGGTTTGCTACAACATGGGCT-3'
CXCL2	F- 5'-AGGGAATTCACCTCAAGAACATCC-3' R- 5'-TGTGGCTATGACTTCGGTTTGG-3'
RPL13A	F- 5'-CAAGCGGATGAACACCAAC-3' R- 5'-TGTGGGGCAGCATACCTC-3'
ACTB	F- 5'-CATCGAGCACGGCATCGTCA-3′ R- 5′-TAGCACAGCCTGGATAGCAAC-3′.

1414

1415 **Extended Data Table 5.**

1416 Data collection and refinement statistics (molecular replacement).

	I325N human (PDB code 5V3P)	WT human (PDB code 5V3B)	WT mouse (PDB code 5DQ6)
Data collection			
Space group	$P3_1$	$P2_1$	$P3_2$
Cell dimensions			
a, b, c (Å)	81.9, 81.9, 297.3	98.7, 80.9, 153.4	71.3, 71.3, 143.2
a, b, g (°)	90.0, 90.0, 120.0	90.0, 102.5, 90.0	90.0, 90.0, 120.0
Resolution (Å)	2.5-40.6 (2.50-2.55) [a]	3.0-34.56 (3.0-3.10) [a]	2.80-37.77 (2.80-2.93) [a]
R_{pim} (all I+ & I-) [b]	0.076 (0.471)	0.056 (0.687)	0.033 (0.398)
$I/s(I)$	7.8 (2.2)	9.9 (1.5)	12.0 (1.42)
$CC_{1/2}$	0.929 (0.713)	0.994 (0.703)	0.996 (0.782)
Completeness (%)	99.7 (100.0)	97.7 (99.1)	96.07 (98.30)
Redundancy	4.5 (4.6)	5.3 (5.6)	4.3 (4.3)
Wilson B ($Å^2$)	47.7	79.0	90.8
Refinement			
Resolution (Å)	2.50-39.47	3.0-34.56	2.8-37.77
No. reflections	73040	44077	19279
R_{work} / R_{free}	0.161/0.200	0.238/0.282	0.253/0.291
No. atoms			
Protein	17465	14207	5511
Water	21	-	26
B factors average			
Protein	55.4	77.3	122
Water	23.4	-	109
R.m.s. deviations			
Bond lengths (Å)	0.0115	0.0117	0.011
Bond angles (°)	1.54	1.53	1.43

1417